Morphological and Functional Ultrashort Echo Time (UTE) Magnetic Resonance Imaging of the Human Lung

Morphologische und funktionelle Magnetresonanztomographie der menschlichen Lunge mit ultrakurzen Echozeiten (UTE)

Doctoral thesis for a doctoral degree
at the Graduate School of Life Sciences,
Julius-Maximilians-Universität Würzburg,
Section Biomedicine.

submitted by

Lenon Mendes Pereira

from

Cruzeiro do Oeste

Würzburg, 2019

cc BY ND

Members of the Promotionskomitee

Chairperson: Prof. Dr. Michael Sendtner
Primary Supervisor: Prof. Dr. Herbert Köstler
Supervisor (Second): Prof. Dr. Michael Laßmann
Supervisor (Third): Dr. med. Thorsten Klink
Supervisor (Fourth): Dr. med. Simon Veldhoen

Date of Public Defence: ……………………………………………………………

Date of Receipt of Certificates: ……………………………………………….

Submitted on: ………………………………………………………………….
Office stamp

“It takes no compromise to give people their rights.
It takes no money to respect the individual.
It takes no political deal to give people freedom.
It takes no survey to remove repression.”
Harvey Milk

Contents

1 Introduction 9

  1.1 Motivation and aim of this thesis 9

  1.2 Thesis outline 13

2 Theory 15

  2.1 The human lung 15

    2.1.1 Lung function and morphology 15

    2.1.2 The mechanics of breathing 19

  2.2 Unenhanced visualization of the lung's parenchyma with MRI 21

    2.2.1 Relevant aspects of Lung MRI 21

    2.2.2 Ultrashort echo time MRI (UTE) 23

  2.3 Magnetic Resonance Imaging of the respiratory motion 27

    2.3.1 Breathing motion and respiratory signal 27

    2.3.2 Real-time navigators 31

  2.4 Unenhanced ventilation assessment with MRI 35

    2.4.1 Fourier Decomposition 37

    2.4.2 Matrix Pencil Decomposition 39

    2.4.3 Self-gated Non-Contrast-Enhanced Functional Lung imaging (SENCEFUL) 41

3 Methods 47

  3.1 3D-SENCEFUL 49

    3.1.1 3D-UTE sequence and protocol 49

    3.1.2 DC gating 51

    3.1.3 Data binning 53

    3.1.4 Trajectory correction and image reconstruction 55

    3.1.5 Ventilation quantification 57

  3.2 2D-SENCEFUL 59

  3.3 SNR comparison 63

4 Results 65

  4.1 Non-gated reconstruction 65

4.2 Self-gating and morphological images 67
4.2.1 Coil clustering versus manual selection 67
4.2.2 3D-UTE versus 2D-FLASH 71
4.3 Ventilation assessment and quantification 75
4.3.1 2D image registration versus 3D image registration 75
4.3.2 Ventilation assessment and quantification in the control group 77
4.3.1 Ventilation assessment and quantification in a patient 81
5 Discussion 85
6 Conclusion 89
7 Summary 91
8 Zusammenfassung 93
9 References 95
10 List of figures 103
11 List of Tables 105
Acknowledgements 107
Publications 109
Papers 109
Conference Proceedings 109
Affidavit / Eidesstattliche Erklärung 111
Curriculum Vitae 113

1 Introduction

1.1 Motivation and aim of this thesis

The field of medical imaging was born in 1895 with the X-ray discovery by Wilhelm Konrad Roentgen. Almost 125 years later, most of the medical imaging categories are still based on exposure to ionizing radiation [1].

According to the most recent report by the National Health Service, almost 70% of all imaging procedures performed in the United Kingdom, between February 2017 and February 2018, involved some level of exposure to ionizing radiation [1]. Among those, X-ray and Computed Tomography were the most relevant, and accounted for almost 95% of the exams [1].

When compared to X-ray, Computed Tomography comprises a small portion of the procedures [2]. Nevertheless, in countries like the United States, CT accounts for nearly half of the population's collective radiation dose from medical examinations [3].

It has been reported that three anatomical regions (head/neck, thorax, and abdomen/pelvis) account for between 76% and 90% of the all CT examinations [4]. Among those, for young patients, 27% of the scans can be replaced by Magnetic Resonance Imaging [5]. For adults, between 47% and 73% of the CT scans could actually be investigated with MRI [6].

Since 2003, the number of MRI examinations is growing at an average of 12% per year in places like the United Kingdom, surpassing the CT growth and the overall growth of diagnostic imaging modalities [2]. This increasing interest in MRI is not only a consequence of a greater concern with radiation doses, but also a result of the improvement in the technology [7]. New contrast mechanism, improvement in SNR, smarter reconstruction techniques and innovative ways to assess metabolic function justify the MRI relevance in clinical routine [8–11]

There are already a variety of scenarios where MRI can replace imaging techniques based on ionized radiation, especially in the brain and lumbar spine [12,13]. For brain function, MRI usually is the gold standard in the study of neuropsychiatric conditions, and in the evaluation of the interaction of new medicines [14].

MRI still encounters several limitations, including long scanning times, motion artifacts, loud acoustic noise levels during measurements and poor SNR in tissues with short relaxation times. One of the most challenging applications is lung imaging, where most of the above problems are found [15].

The treatment and management of pulmonary diseases still rely on ionizing radiation. However, exposure to radiation is detrimental, especially for pediatric patients or when repeated examinations are required, for example, for monitoring chronic pulmonary diseases.

With a combination of extremely short measurement times (that can be performed in a single breath hold) and high-resolution three-dimensional images with sub-millimeter voxel size, Computed Tomography is still the gold standard for the visualization of lung morphology in the field of medical imaging [16].

Conventional pulmonary CT does not provide functional information. Lung ventilation and perfusion is feasible when using dual-energy CT scanners [17]. This procedure is still in the early stages of validation and requires administration of iodine or xenon as contrast agents.

Lung function assessment has been traditionally the hallmark of nuclear medicine techniques. Single-proton emission Computed Tomography (SPECT), and Positron Emission Tomography (PET) represent methods of choice to regionally assess lung ventilation and perfusion [18,19]. Yet, they all require injection of radioactive tracers, which also expose the subject to ionizing radiation.

In this context, magnetic resonance imaging presents itself as a radiation-free modality that can visualize both lung function and morphology. Dynamic contrast-enhanced MRI (DCE-MRI) for example, has better sensibility than SPECT for diagnostic of chronic thromboembolic pulmonary hypertension (CTEPH) and according to Ref. [20], DCE-MRI should be considered as a first-line imaging modality for CTEPH screening.

Unenhanced and non-invasive MRI techniques have also been presented and they allow for the visualization of lung function without administration of any contrast agent. Approaches like Fourier Decomposition MRI (FD-MRI) and Self-gated non-contrast-enhanced functional lung MRI (SENCEFUL) utilizes fast acquisition techniques to monitor the lung proton signal change during free breathing [21,22]. Subsequently, the amplitude of these signal changes is used to quantify regional ventilation and perfusion. Due to limitations of the acquisition methods, FD-MRI and SENCEFUL offer structural images with poor SNR and low spatial resolution.

The perpetual improvement in hardware and software has led to the development of faster MRI sequences, like Ultrashort Echo Time (UTE) and Zero Echo Time (ZTE), which are suited for the detection of signal from tissues with short T2 and T2* components and are naturally robust to movement artifacts [23–25] . UTE and ZTE are promising methods that could resolve the remaining issues in lung MRI, offering morphological images of the lung with both high SNR and spatial resolution.

Theoretically, by combining short echo time acquisitions with an unenhanced method for ventilation and perfusion, it would be possible to create a technique that is able to measure highly resolved images of the lung and assess lung function in a single measurement. This scenario would not only be important from a technological perspective, but also from a clinical point of view, because MRI could become an alternative, or even a substitute, for Computed Tomography, SPECT and PET examinations of the lung.

For this to become a reality, several technical challenges must be overcome. First, fast acquisition techniques can only be as fast as allowed by the scanner hardware, so the MRI sequence must consider the hardware limitations. Additionally, the total measurement time cannot be accommodated in a breath hold and gating and imaging registration techniques must be implemented to account for breathing and cardiac motion.

After measurement, the data, which would probably be undersampled in order to reduce the measurement time, must be reconstructed and the functional contrast extracted using signal models.

With that in mind, this work proposes the implementation of a 3D Ultrashort Echo Time sequence in the Self-gated non-contrast-enhanced functional lung MRI framework. For this reason, a 3D-UTE sequence was developed and implemented on a 3 Tesla MRI scanner.

The new sequence was used to acquire morphological images with high resolution in 6 healthy subjects and a patient with lung cancer. The study was performed in free-breathing and without administration of contrast.

After measurement, time-resolved images of the breathing cycle were reconstructed using iterative SENSE. An automatic technique for gating, using a combination of the signal from different coil arrays was evaluated.

The breathing motion was then suppressed using a two-dimensional and a three-dimensional image registration technique, and the results of the two algorithms were compared.

Ventilation-weighted maps were generated with SENCEFUL, and regional ventilation was quantified. In the end, the results of the 3D-UTE implementation were compared with the standard SENCEFUL approach.

1.2 Thesis outline

This work is structured as follows:

Chapter 2 presents an overview of the morphology and function, with a focus on the ventilation process and breathing motion. The challenges of lung magnetic resonance imaging are discussed, and a technique for fast image acquisition is presented. The state of the art for self-gating techniques and unenhanced ventilation assessment are also examined.

Chapter 3 outlines the methods used in this study, including the acquisition technique, gating, reconstruction and extraction of the functional information from the lung.

Chapter 4 contains the results of this work, with quantitative values for ventilation and ventilation-weighted maps. A comparison with a standard method for ventilation assessment is presented.

The results are discussed in Chapter 5, and in Chapter 6 and 7 a brief conclusion and summary of the findings can be found.

2 Theory

2.1 The human lung

2.1.1 Lung function and morphology

The organs of respiration can be divided into three sub-systems: the upper airways (nasal and oral cavities, nasal sinuses, pharynx), lower airways (trachea, alveoli and bronchial tree) and the respiratory muscles (diaphragmatic and intercostal muscles) [26].

After being filtered in the nasal passages, air passes through the pharynx and larynx, to the trachea. The respiratory tract regulates the air temperature and humidity. The trachea conducts the inhaled air to the bronchi and the exhaled air out of the respiratory system [26]. An illustration of the trachea and bronchial tree is presented in Figure 1.

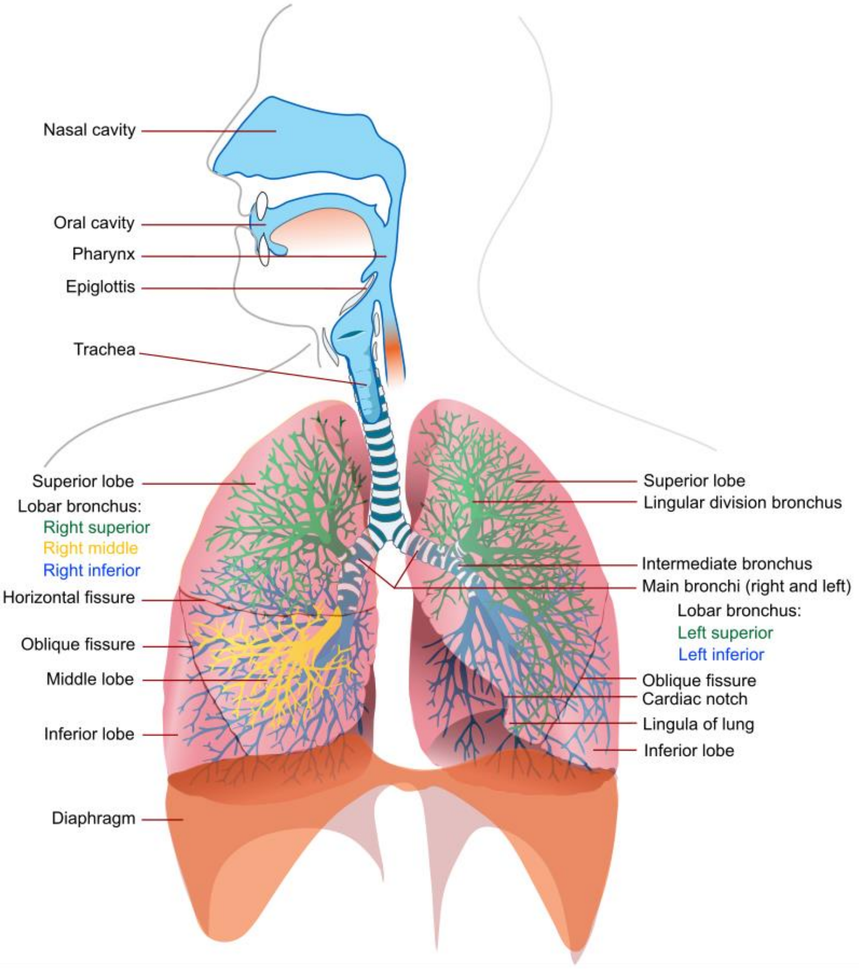
Nasal cavity
Oral cavity
Pharynx
Epiglottis
Trachea
Superior lobe
Lobar bronchus:
Right superior
Right middle
Right inferior
Horizontal fissure
Oblique fissure
Middle lobe
Inferior lobe
Diaphragm
Superior lobe
Lingular division bronchus
Intermediate bronchus
Main bronchi (right and left)
Lobar bronchus:
Left superior
Left inferior
Oblique fissure
Cardiac notch
Lingula of lung
Inferior lobe

Figure 1. Anterior view of the upper and lower airways. Opensource image from Ref. [27].

The right and left bronchi bifurcate from the trachea. The right bronchus is wider, with three main lobes, while the left one is narrower, with only two lobes [28,29]. Each bronchus divides into secondary bronchi, which then is further branched into tertiary bronchi. Bronchioles, with very small diameters, spread repeatedly through the lung from the tertiary bronchi.

Alveolar ducts are connected to the very end of each bronchiole, and each duct branches in approximately 100 alveolar sacs [26]. Each sac is filled with several alveoli, which are in direct contact with the capillaries of the respiratory system [26].

An illustration of the alveoli sacs and capillaries is presented in Figure 2.

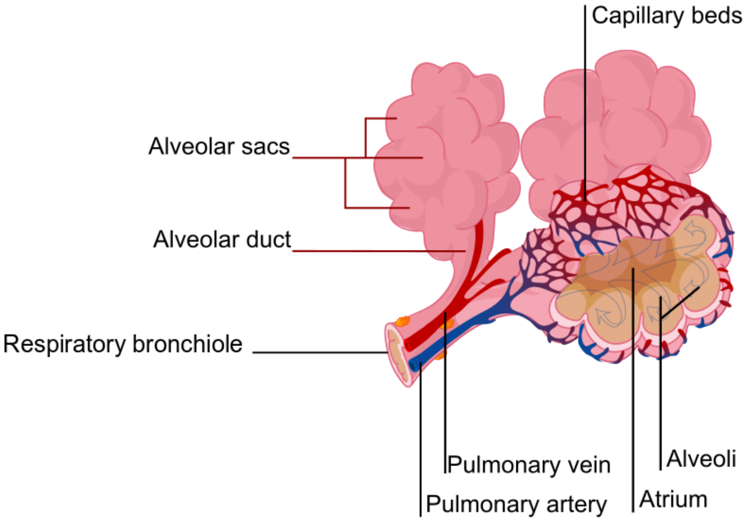

Figure 2. Bronchiole, capillaries and alveoli. Opensource image from Ref. [27].

The pulmonary artery branches and spread throughout the lung similarly to the bronchial tree, decreasing in size and diameter at each dichotomy, while its total cross-sectional area increases. The arteries spread more profusely in the peripherical areas of the alveolar wall, where the capillaries may occupy up to half of its surface (Figure 2) [28]. The two lungs contain about 300 million alveoli, with approximately 100 m^2 of total surface available for gas exchange [28].

The gas exchange happens through passive diffusion, across the pulmonary blood-gas barrier at the alveolar membrane [30]. This is a continuous process, involving both ventilation and perfusion [30].

The capillaries in the alveolar wall are irrigated with arterial blood, which has a low concentration of oxygen (O_2) and a high level of carbon dioxide (CO_2) [30]. This causes a change in partial pressure, from the alveoli to the capillaries. The high concentration of O_2 in the capillaries drives the O_2 into the tissue. And the high amount of CO_2 in the capillaries drives the CO_2 into the alveoli.

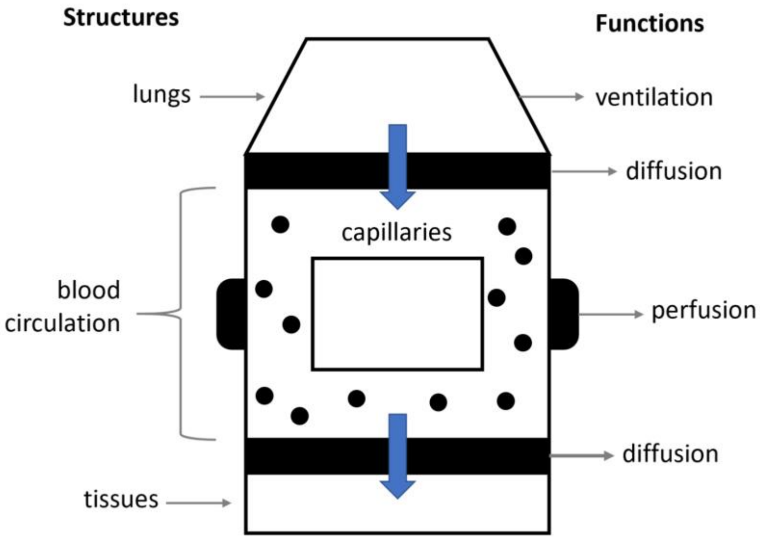
Structures
Functions
lungs
ventilation
diffusion
capillaries
blood circulation
perfusion
diffusion
tissues

Figure 3. Schematic of the oxygen transport pathway showing the principal structures and their physiological functions. Adapted from Ref. [30].

After the blood has flowed through the capillaries and has reached the pulmonary veins, O_2 levels are increased and CO_2 levels decay [30].

It can be assumed that ventilation is the circulation of air in and out of the lungs, and perfusion is the blood flow in the pulmonary capillaries. When ventilation is higher than perfusion, the arterioles expand and the bronchioles constrict. Similarly, when perfusion is higher than ventilation, the arterioles constrict, and the bronchioles expand. Imbalances are usually caused by diseases or the regional gravity effect on blood [30].

2.1.2 The mechanics of breathing

The main function of the human lung is to enable the exchange of oxygen and carbon dioxide between the alveolar and pulmonary capillary [26]. As previously explained, gas exchange is continuous and involves both ventilation and perfusion. For that to occur, the lung must be constantly ventilated. The alternation between inspiration and expiration ensures that fresh air will get in contact with the alveoli and the excess of carbon dioxide will be removed from the body. This gas exchange is made possible by pressure differences between the lungs and the atmosphere.

To enable these pressure differences, the volume of the lungs is increased during inspiration and decreased during expiration. The diaphragm takes the main role in this process, which is also supplemented by thoracic respiration.

For inspiration, the diaphragm and intercostal muscles must overcome the elastic resistance in the lung and chest wall, as well as the viscous resistance in the airways. During tidal breathing, 75% of the intrathoracic volume changes due to diaphragmatic breathing [26,29]. When the diaphragm contracts, the space between the diaphragm and the chest wall is then filled by the lung. Thoracic respiration is more active during forced breathing. In thoracic respiration, the external intercostal muscles elevate the obliquely placed ribs, which expand the chest cage [26,29].

Because of its elastic nature, the lungs normally tend towards the reduction of their volume. Thus, expiration is considered a passive process, where the energy accumulated during inspiration is released from the elastic fibers of the lung and the diaphragmatic muscles, forcing air out the body while the chest cage returns to its resting position [26]. During forced exhalation, the abdominal muscles exert additional pressure, enhancing the movement.

The amount of gas in the lungs is measured in terms of lung volume and lung capacity. Lung volume measures the amount of air in a single function [31]. For example, tidal volume (TV) is the volume of air inhaled in a single breath during normal breathing.

Lung capacity measures the sum of two or more volumes. The vital capacity (VC), for instance, represents the amount of air that can be inhaled during a breathing cycle, and it's calculated as the sum of the expiratory reserve (ERV), tidal and inspiratory reserve (IRV) volumes [31]. An illustration of the correlation among different values of lung capacity and lung volume is found in Figure 4.

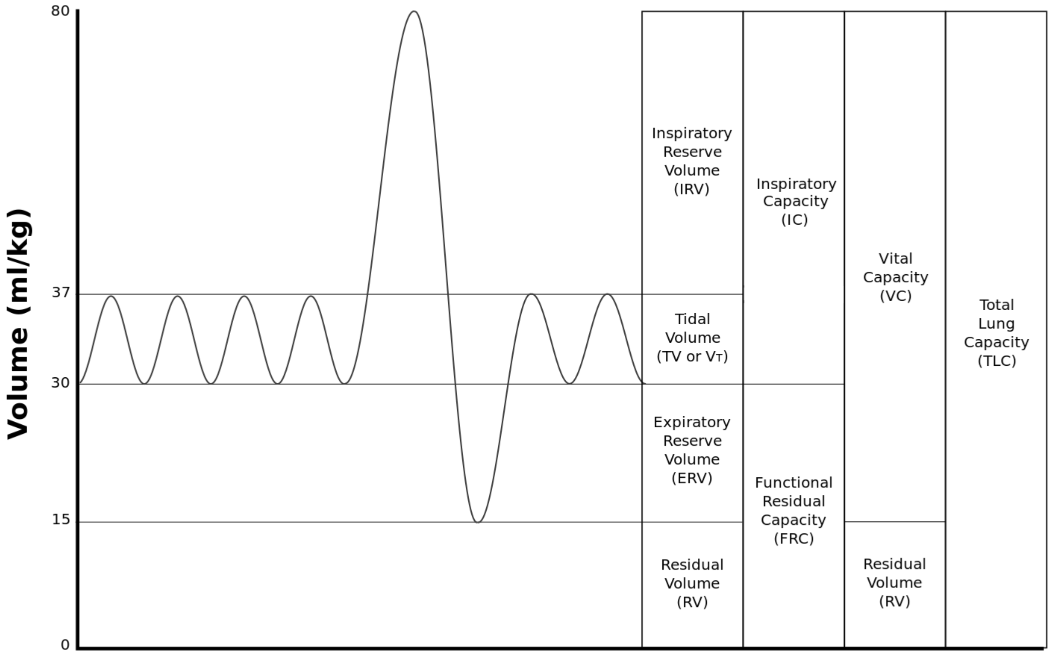
Volume (ml/kg)
80
37
30
15
0
Inspiratory Reserve Volume (IRV)
Tidal Volume (TV or V_T)
Expiratory Reserve Volume (ERV)
Residual Volume (RV)
Inspiratory Capacity (IC)
Functional Residual Capacity (FRC)
Vital Capacity (VC)
Residual Volume (RV)
Total Lung Capacity (TLC)

Figure 4. Standard lung volumes and capacities from a spirometer trace [31].

Lung volume and size depends on age, sex, body build, and physical conditioning. The normal TV in adults is usually 10% of VC, approximately 300 – 500 ml [32]. During exercise, TV can increase up to 50 % of VC [33].

Pulmonary function tests (PFT) are the gold standard to measure lung volume, function and capacity. Spirometry is the most clinical adopted PFT and directly measures changes in lung volume by monitoring the amount and rate of air expired by the lungs over time. However, this method is relatively insensible, as it analyses ventilation only on a global scale, without any regional information.

2.2 Unenhanced visualization of the lung's parenchyma with MRI

2.2.1 Relevant aspects of Lung MRI

When using magnetic resonance to image the lung, there are some intrinsic properties that must be considered. The most important ones are low proton density, local magnetic field inhomogeneities, short T2* times and continuous motion.

The lung parenchyma has very low proton density, between 0.1 and 0.3 g/cm^3 (depending on the level of inflation), which is about ten times less than other tissues in the human body. For comparison, the density of the human cerebrum is on average 1.04 g/cm^3 and of the liver is about 1.05 g/cm^3 [34,35]. As a result, the MR signal from the parenchyma is much lower than in the adjacent tissues.

The lower proton density is explained by the high number of airways and alveoli that are present in the lung and are required to achieve a larger surface area for gas exchange. These heterogeneous structures (Figure 5) result in microscopic magnetic field inhomogeneities, caused by the different magnetic susceptibility of the lung tissue and the air.

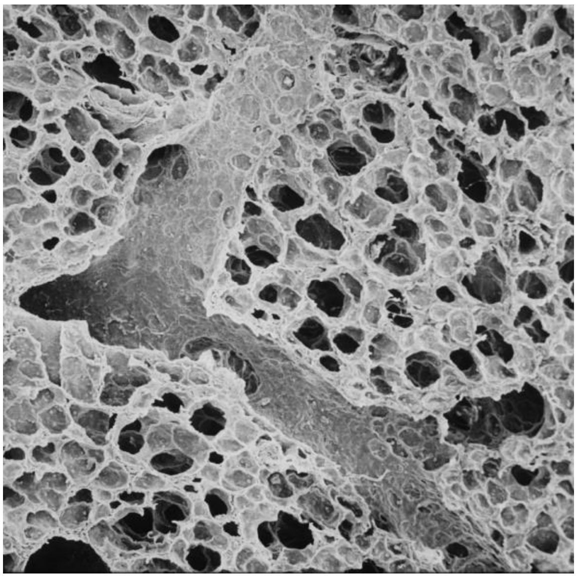

Figure 5. Microscopic image of the lung parenchyma [36].

Magnetic field inhomogeneities lead to fast dephasing of the already low MR signal, resulting in extremely short T2* values. Higher B_o intensities attenuate local magnetic inhomogeneities, shortening the T2* even more at higher field strengths. This behavior leads to a trade-off between signal amplitude and T2* values, because even though the MR signal is higher at higher B_o fields, its signal also decays faster, which requires even faster acquisition techniques. Ref. [37] compared the lung T2* during free-breathing at 1.5 and 3 T, and found a reduction of 75% for the T2*, from 2.11 ± 0.27 ms at 1.5 T to 0.74 ± 0.1 ms at 3T.

Moreover, continuous motion in the thorax and abdomen require countermeasures to avoid image blurring.

2.2.2 Ultrashort echo time MRI (UTE)

Ultrashort echo time techniques represent the method of choice when high SNR and improved image resolution from the lung parenchyma are sought [38]. They minimize the effect of rapid signal decay in the lung by reducing the echo time to less than 200 microseconds [39,40]. This is normally achieved by sampling the free induction decay as soon as possible, right after the radiofrequency (RF) excitation.

UTE can be used for both 2D and 3D measurements, and it's based on non-cartesian trajectories, like radial-center out and spirals [41,42]. In this work, only radial-center out trajectories will be discussed.

In a conventional Cartesian approach, the k-space is filled line by line. In radial center-out, every readout starts at the k-space center and then the system is rotated. For reference, a schematic of the k-space trajectory in Cartesian and radial acquisitions is presented in Figure 6.

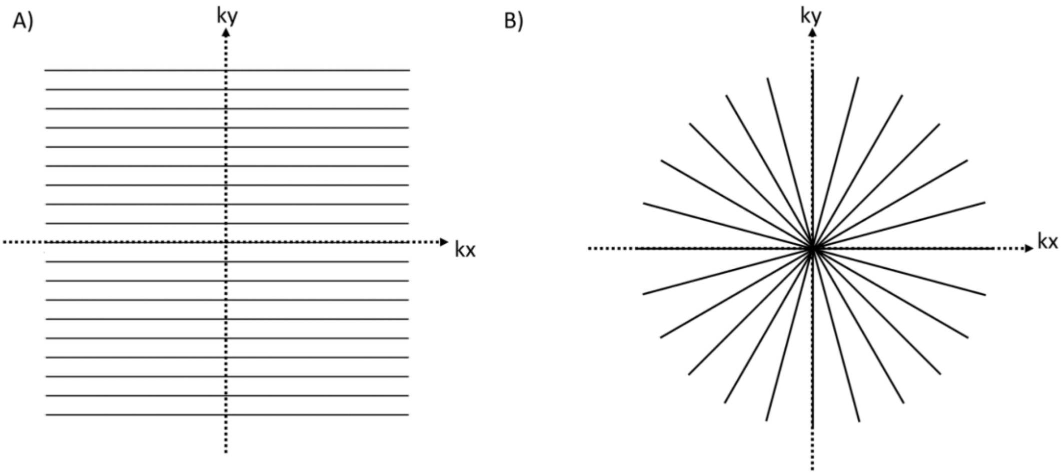

Figure 6. Two dimensional cartesian (A) and radial (B) k-space trajectories.

In radial acquisitions, any given direction in the k-space can be characterized by the polar angle ($0 < \Theta < \pi$) and the azimuthal angle ($0 < \phi < 2\pi$) [43]. In a three-dimensional k-space, the x, y and z components of the readout gradient G can be calculated according to the following set of equations:

$$\begin{aligned} G_x &= G\ \sin\Theta\cos\phi \\ G_y &= G\ \sin\Theta\sin\phi \\ G_z &= G\cos\phi \end{aligned} \qquad \text{Equation 1}$$

Radial acquisition results in a non-uniform sampling of the k-space, with oversampling of the lower frequencies. Moreover, UTE radial methods sample the k-space while the gradients are being ramped up, resulting in a non-linear sampling. Re-gridding algorithms and weighting functions are then required during image reconstruction to correct such nonuniformities [39,44].

The Nyquist criterium requires that the distance between adjacent samples, in the k-space, should be less than the inverse of the image FOV. As demonstrated by Ref. [43], the number of half-echo acquisition required to fulfill the Nyquist sampling rate in a sphere enclosing volume is:

$$N_{proj} = 4\,\pi\,{k_{max}}^2 \qquad \text{Equation 2}$$

In order to meet the Nyquist criterion also in the periphery of the k-space, three-dimensional radial acquisitions require π times more the number of readouts compared to a 3D cartesian method with a similar matrix size. This increases the total acquisition time and creates raw data sizes that are computationally challenging to handle [45,46]. On the other hand, radial trajectories are naturally more robust against under sampling, so reaching full Nyquist in the outer parts of the k-space is not always necessary [47].

For 2D-UTE applications, half excitation pulses are typically used, and the slice profile results from a sum of two excitations with opposing gradients [37]. There is no slice selection for 3D imaging, hence an even shorter TE can be achieved, as the data is sampled a few microseconds after the end of the RF pulse. An example of a 2D and 3D UTE techniques is displayed in Figure 7.

.

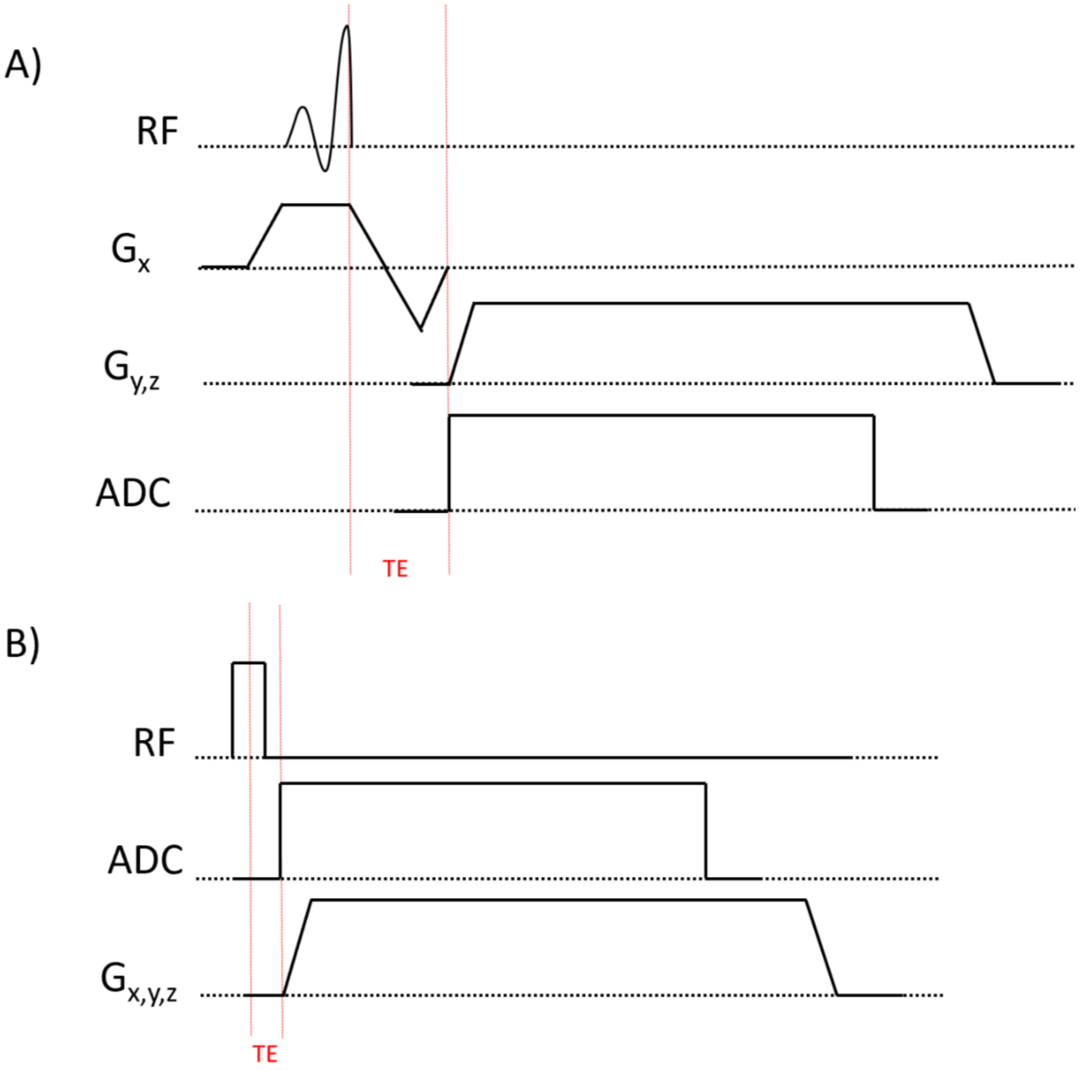

Figure 7. Ultrashort echo time sequences diagrams for 2D (Fig. A) and 3D (Fig. B) acquisitions. 2D-UTE normally uses a half-pulse excitation, which is applied with the slice selective gradient. 3D-UTE normally employs a rectangular hard-pulse excitation. For both, the sampling starts while the gradients are still ramping up.

In short echo time acquisitions, the echo time is mainly limited by the hardware dependent dead-time, which is defined as the delay between the end of the RF pulse and the beginning of the data acquisition [48,49]. The dead-time is related to the ADC filtering, the circuit ring down time and the switching of the coils from transmitter to receiver mode.

Radial acquisitions are very sensible to gradient delays and imperfections, therefore, corrections are also required. As reported by Ref. [45], hardware imperfections might cause offsets between the start of the readout gradient and the ADC sampling. Consequently, the data must be re-grid at the k-space center and on the ramp, to avoid image artifacts during reconstruction [45].

In contrast to the read direction in conventional Cartesian imaging, the signal from outside the encoded area can create aliasing artifacts, which are usually manifested as streaks and blurring [39,40,44]. Thus, it is recommended to use RF coils with sensitivities limited to the desired FOV.

For pulmonary applications, besides the reduction of signal loss, radial sampling schemes are also naturally less sensitive to motion artifacts [50]. As demonstrated by Ref. [50], the over-sampling of low-frequencies components, responsible for gross features and contrast, results in the reduction of motion artifacts and offers similar benefits to conventional signal averaging.

Additionally, the center of the k-space can be used to monitor physiological functions, such as cardiac and respiratory motion. Consequently, UTE acquisitions are gaining attention in the past few years for their inherent self-gating ability. [51].

UTE can also provide similar contrast and diagnostic information as in Computed Tomography, with isotropic resolution as small as 1 mm [51]. In combination with hyperbolized gasses and oxygen-enhanced MRI (OE-MRI), UTE is a promising method to evaluate disease progressions without multiple exposures to radiation [40].

2.3 Magnetic Resonance Imaging of the respiratory motion

2.3.1 Breathing motion and respiratory signal

As observed by Ref. [52], the signal intensity in the parenchyma depends on the state of inflation of the lung. During expiration, for example, the lung contracts and the relative proton density in a voxel is increased, reducing the magnetic susceptibility and increasing the MR signal intensity. Consequently, the proton density of the parenchyma is determined by the phase of the respiratory cycle and is directly correlated with lung volume [21].

By observing the diaphragm motion in fluoroscopic studies, Ref. [53] proposed an equation (Equation 3) to estimate its position over time.

$$z(t) = z_0 - bcos^{2n}\left(\frac{\pi t}{\tau} - \varphi\right) \qquad \text{Equation 3}$$

where z_0 is the position at exhale, *b* is the amplitude of the respiratory cycle, *n* determines the steepness and flatness of the curve, φ is the phase of the respiratory cycle and τ is the period of the respiratory cycle. An example of *z(t)* is presented in Figure 8, for τ = 5 s, b = 2 cm and n = 3.

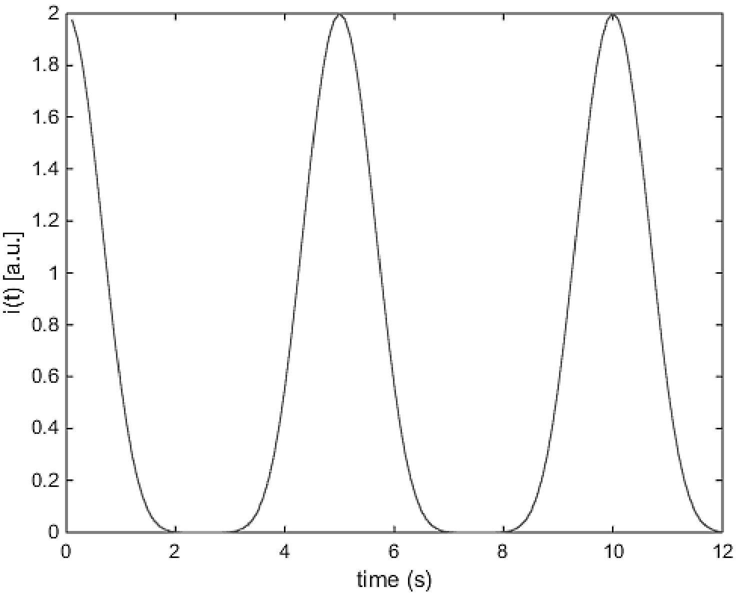

Figure 8. Simulation of the position of the diaphragm.

Ref. [21] modified Equation 3 to include the contribution of cardiac motion to the MR signal, which is a result of the blood flow in the ventricles.

$$i\,(t) = i_o - A_r cos^{2n}\left(\frac{\pi t}{\tau_r} - \varphi_r\right) + A_c cos^{2m}\left(\frac{\pi t}{\tau_c} - \varphi_c\right) \qquad \text{Equation 4}$$

where i(t) is the signal variation with respect to the cardiac and breathing cycles, i_o is a constant value for the signal's baseline, τ_r and φ_r are the period and phase of the respiratory cycle, τ_c and φ_c are the period and phase of the cardiac cycle, A_r and A_c are the amplitude of the respiratory and cardiac cycles, and *n* and *m* affect the shape of the curve.

A simulation of the respiratory and cardiac time-courses is presented in Figure 9 using A_r = 10, A_c = 5, τ_r = 5 s, τ_c = 0.8 s, n = 3, m = 1 and i_o, φ_r, and φ_c = 0.

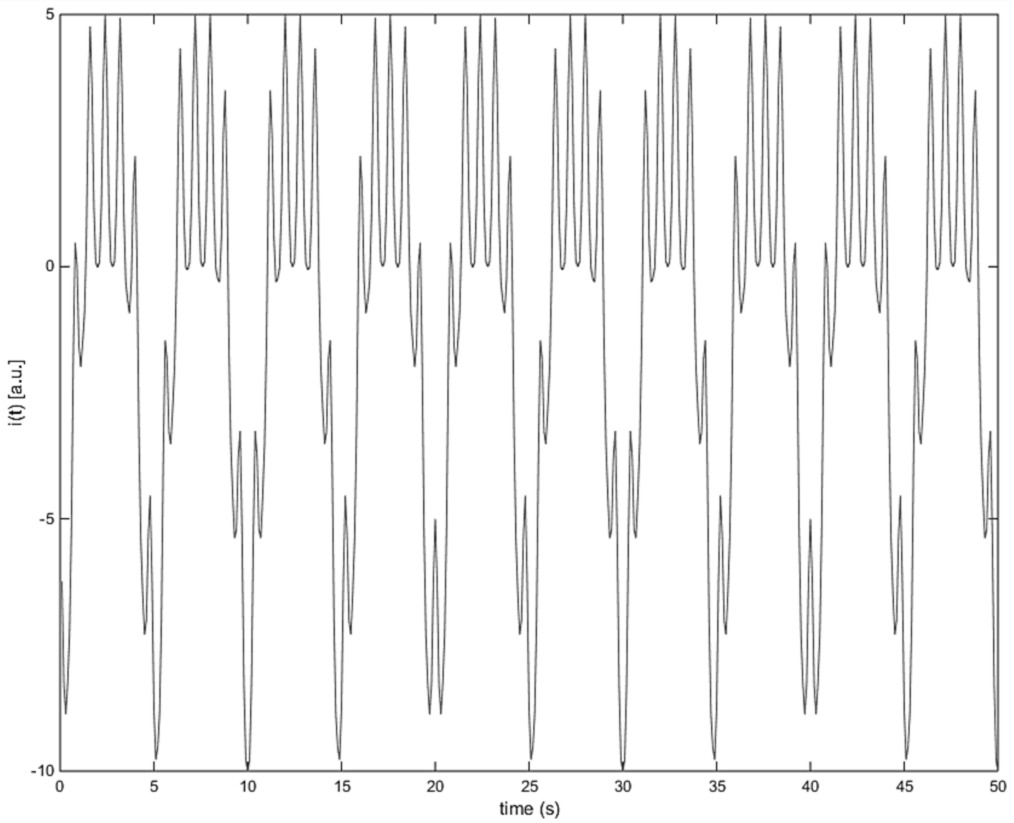

Figure 9. Simulation of the contribution of the cardiac and breathing motions to the MR signal.

After applying a Fourier transform, it is possible to observe the frequency components related to each motion in the Fourier domain (Figure 10).

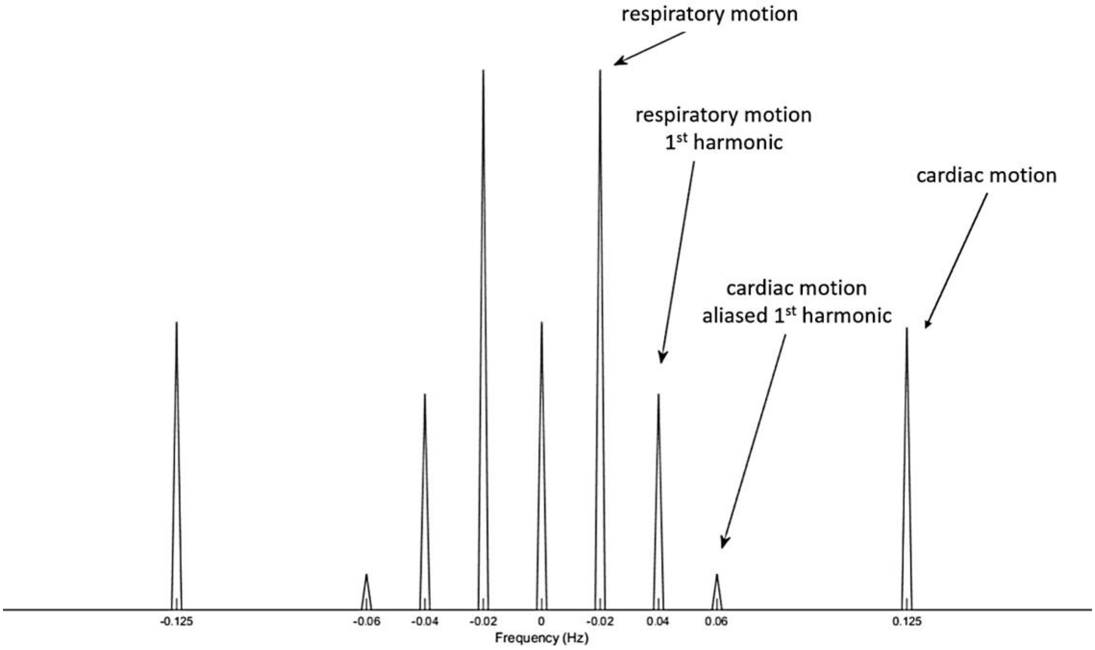

Figure 10. Spectral separation of the cardiac and breathing motions in the frequency domain.

In adults, the average cardiac frequency is between 0.75 and 2 Hz, corresponding to beating rates of 45 to 120 beats per minute. Breathing frequencies range, on average, between 0.1 and 0.5 Hz, corresponding to one respiratory cycle every 2 - 10 seconds [22]. Spectral separation of the cardiac/respiratory motion contribution to the MR signal can be achieved using high and low pass filters [21].

2.3.2 Real-time navigators

Magnetic resonance imaging of the respiratory motion, in free-breathing, requires synchronization of the image acquisition with a navigator that represents the respiratory cycle. This can be achieved using external devices (i.e. thoracic belts, bellows or cushions) or using self-gated MRI techniques.

External devices monitor the chest or abdomen expansion and are mainly used for prospective gating, meaning that the data acquisition only happens when a specific state of expansion is reached (normally end-expiration). Bellows for respiratory synchronization have also been used for retrospective gating [54]. Nevertheless, these devices reflect only the motion patterns of the chest wall and do not offer a direct representation of the respiratory motion [55].

Self-gating (SG) techniques, on the other hand, do not rely on external devices, because the information related to respiratory motion is extracted from the measured MR data itself. SG methods can be classified into two distinct groups: Image-based self-gating (Img-SG) and DC self-gating (DC-SG).

Img-SG relies on the direct visualization of the breathing motion, by reconstructing images with low spatial resolution [56]. For that, sequence parameters must be within the limits imposed by the characteristics of the movement of interest, in order to maintain acceptable spatial and temporal resolutions [56]. The use of a sliding window approach, partially overlapping adjacent datasets, can be helpful to improve temporal/spatial resolution.

In lung imaging, the liver-lung interface is the most common monitored area. As previously discussed, the movement of the diaphragm offers a very good approximation of the lung motion. Thus, by monitoring its displacement over time, it is possible to create a signal navigator based on its position. This approach is demonstrated in Figure 11 and Figure 12.

In Figure 11, low-resolution reconstructions from a radial center-out acquisition are presented. Each image was reconstructed with only 700 radial samples, using a sliding window approach. The number of radial samples is not sufficient to fully sample the k-space, but it provides enough information to detect the position of the diaphragm over time.

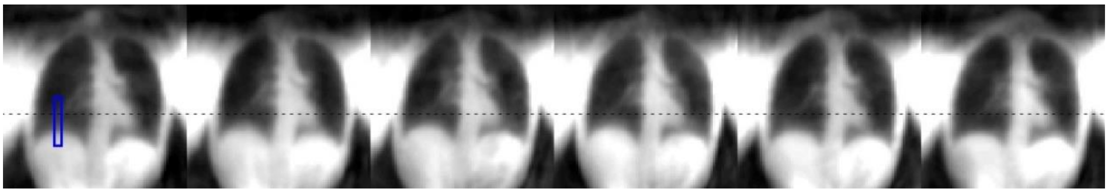

Figure 11. Breathing phases reconstructed using an Img-SG approach.

The displacement of the lung-liver interface, monitored in the region of interest tagged with a blue rectangle in Figure 11, is presented below.

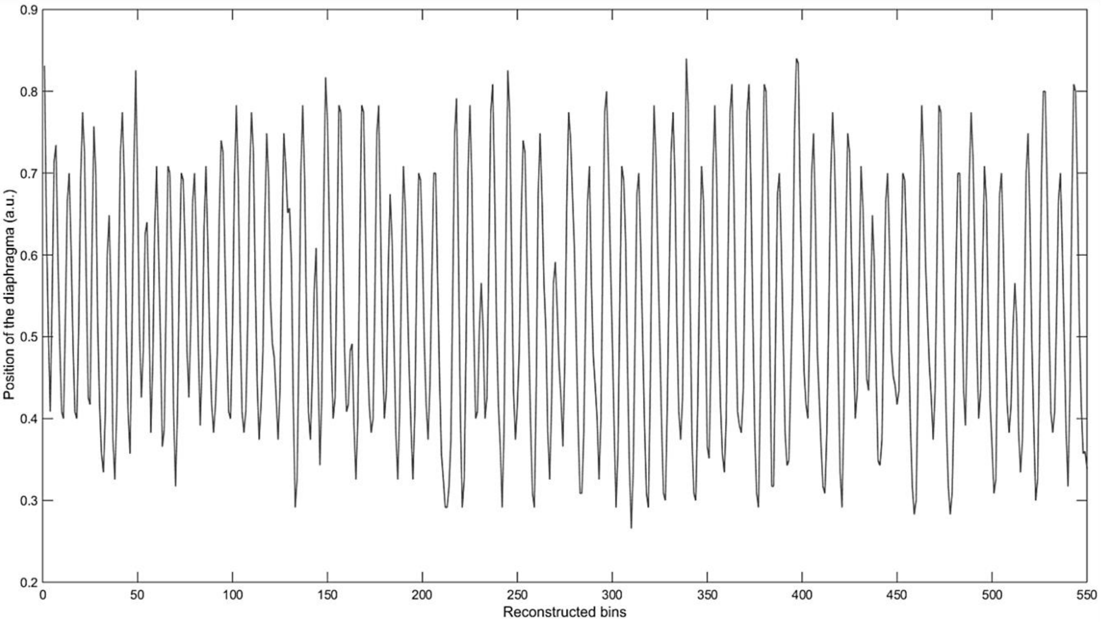

Figure 12. The position of the diaphragm during a free-breathing measurement monitored with an Img-SG approach

DC-SG does not require any image reconstruction to extract the SG signal. In this case, the k-space center, which represents the sum of the total transverse magnetization in the excited region, is used as a navigator. In 2D acquisitions, the movement of an object within the slice region changes the spin density, which leads to DC signal variations. A similar effect is observed when the blood flow carries unsaturated spins into the excited region, causing changes in the overall magnetization and in the DC signal [57].

In 3D measurements, the whole volume is excited, minimizing the effect caused by the inflow of unsaturated spins. Nonetheless, changes in the spin density still cause proportional DC signal variations. Consequently, the movement of the diaphragm in the excited volume will lead to a synchronous signal variation of the DC signal, which can be recorded by coil elements positioned near the diaphragm.

Likewise, coil arrays positioned close to the heart, will be able to record variations caused by cardiac motion. The maximum amplitude of the DC signal for 2D cardiac applications results from the inflow of spins from major vessels or from the blood flow in the ventricles.

In this scenario, radial acquisitions have obvious advantages over cartesian techniques, because they sample the k-space center at every TR. Cartesian methods must be adapted to acquire such information [22].

The DC signal extracted from the k-space center of the previous radial center-out acquisition is visualized in Figure 13.

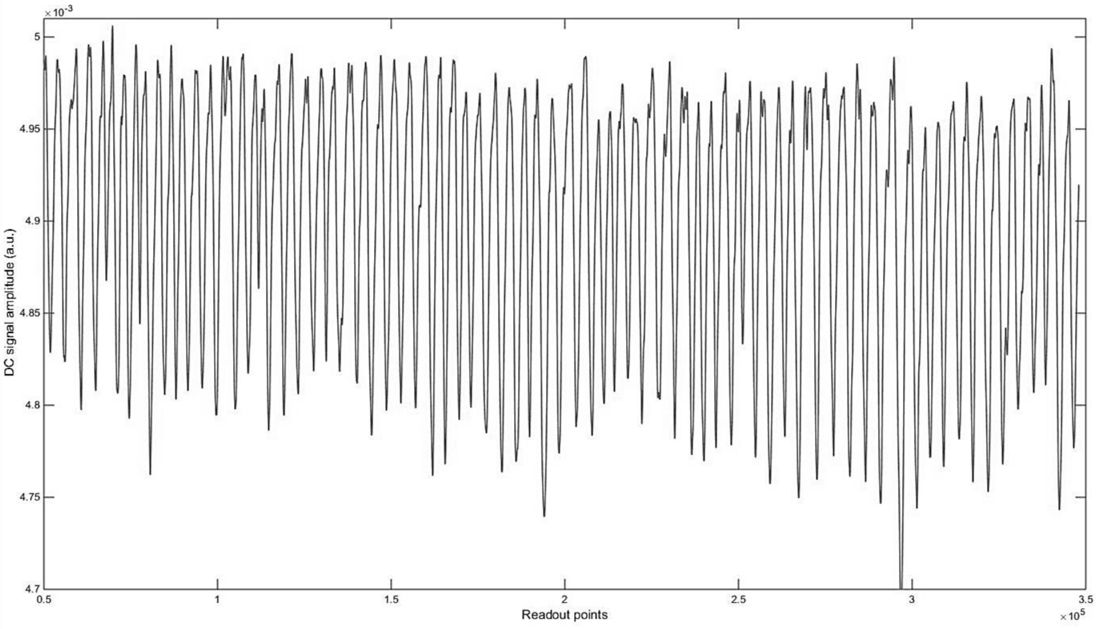

Figure 13. DC signal from a single coil element positioned close to the diaphragm.

The resulting gating information from both Img-SG and DC-SG enables the reconstruction of multiple respiratory phases from a single acquisition, allowing the visualization of the breathing motion and the assessment of lung function.

2.4 Unenhanced ventilation assessment with MRI

Hyperpolarized gasses, like Helium-3 and Xenon-129, have been exploited to evaluate regional inhaled gas density in patients in a few specialized centers. However, their clinical application has been limited by high costs and the requirement of specialized equipment for administration and measurement [58]. Oxygen-enhanced MRI is a cheaper alternative, but low SNR and long acquisition times are obstacles to a broader implementation [59].

Given the limitations of hyperpolarized gasses and oxygen-enhanced MRI, unenhanced techniques like Fourier Decomposition, Matrix Pencil Decomposition, and SENCEFUL are gaining interest as potential alternatives [21,22,60]. A description of each one is presented next.

2.4.1 Fourier Decomposition

Fourier Decomposition MRI was first introduced by Ref. [21] as a method to obtain regional lung ventilation and perfusion in free breathing and without the administration of contrast agents. FD-MRI, in its original implementation, employs a two-dimensional balanced steady-state free precession (bSSFP) pulse sequence to acquire time-resolved sets of lung images.

Normally, between three and five images are acquired per second. Subsequently, the time series is registered to a reference image with a mean value of the diaphragm position by using a non-rigid two-dimensional registration algorithm. This eliminates most of the signal changes caused by motion and guarantees that the signal alterations in the image stack will be a result of spin density and input variations. For ventilation, the expansion and contraction of lung parenchyma lead to these signal variations. While for perfusion, the main responsible for signal changes is the inflow caused by the cardiac motion.

The signal contributions of perfusion and respiration can be spectrally separated by a pixel-wise Fourier transform along the temporal dimension. Therefore, integration over the range of frequencies related to perfusion/ventilation is applied in the Fourier domain, to produce functional information. Hence, unsteady breathing and cardiac motion cause widening of the spectral lines, which can lead to undesired noise and artifacts [21].

Another particularity of the Fourier transform approach is that non-oscillating signals do not have a frequency component. So, in cases where the blood flow is constant during measurement, its frequency component is transferred to the 0-Hz in the Fourier domain. As a result, it won’t appear on the perfusion maps [61]. Its indirect approach to picture ventilation is also not able to show the alveolar and bronchial space, as with hyperpolarized gas imaging, due to a lack of regional changes in proton density [61].

Additionally, the 2D-bSSFP (or any other 2D technique) suffers from through-plane motion artifacts [62]. Partial volume effects, caused by a large slice thickness, have also been reported [21,61,63].

Fourier decomposition has presented results in agreement with traditional methods, such as dynamic contrast-enhanced MRI (DCE-MRI), single proton emission computed tomography (SPECT) and dynamic fluorinated gas washout MRI (^{19}F-MRI) [21,61,63]. In Figure 14, Ref. [21] compared perfusion weighted images from FD-MRI with dynamic contrast-enhanced MRI, from a patient with cystic fibrosis (DC-MRI).

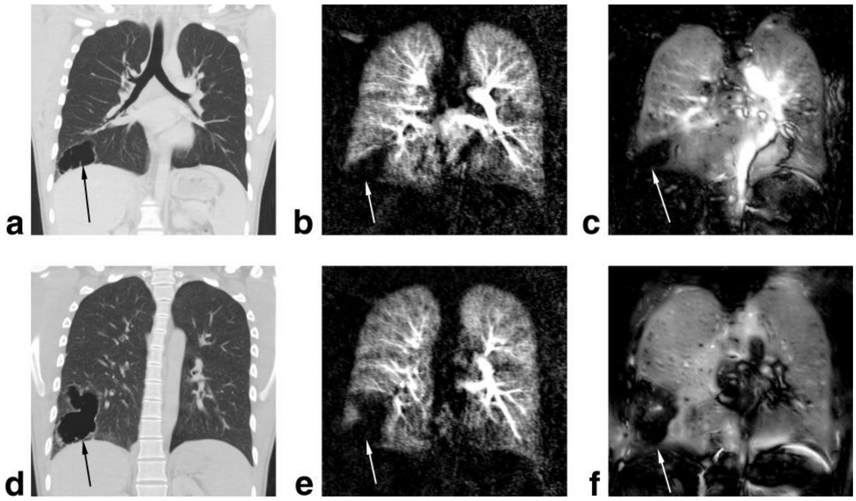

Figure 14. Morphological CT in coronal view (a,d) and perfusion maps of a patient with a cystic parenchymal defect in the lower lobe of the right lung (arrows) shows a tissue density malformation. A perfusion defect in DCE-MRI perfusion map (b,e) is clearly visible on the perfusion-weighted image (c) and density-weighted image (f) obtained using the Fourier decomposition method. Ref. [21], used with permission from John Wiley and Sons.

Its clinical potential has also been demonstrated in patients with obstructive pulmonary diseases (COPD) [21,61,63].

2.4.2 Matrix Pencil Decomposition

Besides widening of the spectral lines, FD-MRI also requires stable peak detection in the Fourier spectrum, which has been reported to be very unstable [60]. Furthermore, the Fourier transform of truncated signals often causes spectral leakage and Gibbs ringing artifacts [64]. Ref. [60] proposed the use of a Matrix Pencil method (MP), to better estimate the position of the respiratory and cardiac peaks in the frequency domain. Matrix pencil works on truncated, time-shifted and equidistant data sets, and it has been traditionally used in spectroscopy to estimate the spectral components of a sum of exponential signals [64].

Similar to FD-MRI, a time-resolved image series of the thorax was acquired, using a 2D- bSSFP technique. Spatial inconsistencies in the image stack are corrected with a non-rigid 2D image registration. The signal in a region in the center of the FOV is summed and low and high-pass filters are used to separate its cardiac and ventilation contributions. One matrix with the respiratory poles, and another with the cardiac poles, are then retrieved using the matrix pencil decomposition of the respective low and high-pass-filtered signals. The local respiratory and cardiac amplitudes can then be found voxel-wise by a Moore-Penrose inverse these matrices [60].

When compared to FD-MRI, MP offered a more precise evaluation of the respiratory and cardiac signal modulations in the lung parenchyma [60].

Ref. [60] compared the image quality of ventilation and perfusion-weighted maps measured with FD-MRI and MP. The results are presented in Figure 15.

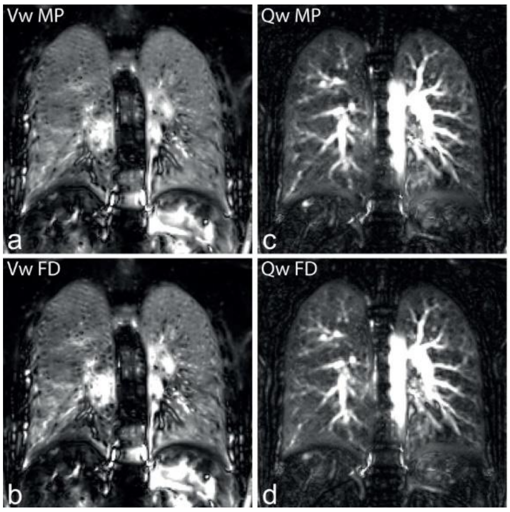

Figure 15 - Ventilation-weighted (Vw) and perfusion-weighted (Qw) images generated with MP (a, c) and standard FD method (b, d). From Ref. [22], used with permission from John Wiley and Sons.

The image quality of the ventilation and perfusion-weighted maps was found to be analogous to FD-MRI. However, quantification of ventilation and perfusion were more accurate. Notwithstanding the improved quantification, widening of the spectral lines is still an obstacle in this method.

2.4.3 Self-gated Non-Contrast-Enhanced Functional Lung imaging (SENCEFUL)

Self-gated Non-Contrast-Enhanced Functional Lung imaging utilizes a DC-SG approach to obtain highly resolved ventilation and perfusion-weighted maps of the human lung in free breathing. In its original implementation, SENCEFUL employs a modified two-dimensional Fast Low-Angle SHot (FLASH) sequence, with a quasi-random sampling order of the k-space, to additionally sample a non-phase-encoded free induction decay (FID) after each readout.

Afterwards, the DC signal from each coil is filtered and coil elements with high sensibility to the cardiac/respiratory motion are selected. The gating signal is used as a reference to re-sort the quasi-random data in different bins, each one corresponding to a specific breathing/cardiac phase from a representative breathing/cardiac cycle.

The respiratory gating using the direct current (DC) signal, extracted from a coil element positioned close to the diaphragm, is presented in Figure 16 (a and b). The periodic motion of the diaphragm is reflected in the resulting DC signal. The signal reaches its highest amplitude during expiration and its minimum during inspiration. A gating window (Figure 16 (c)), is used to separate all data related to a state of motion. This gating window can be shifted along the scope of the DC signal, and different data stacks, corresponding to different breathing phases, can be created and reconstruct. Figure 16 (c) highlights three breathing phases (end-expiration, intermediate respiratory phase and end-inspiration).

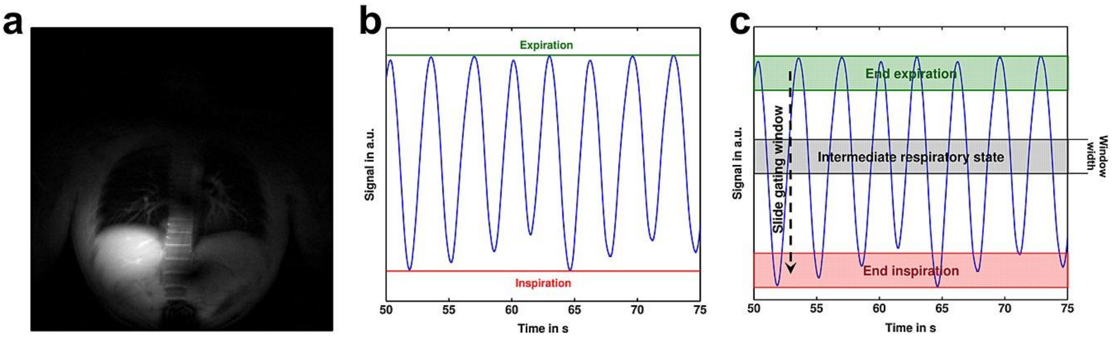

Figure 16. Illustration of the DC signal (b) extracted from a coil element close to the diaphragm (a) and the corresponding gating process (c). From Ref. [22], used with permission from John Wiley and Sons.

This allows for the suppression of the breathing motion and an improved depiction of the lung morphology. Additionally, because the data is sorted into a single pseudo cycle, it solves the problems related to spectral broadening.

A similar approach is used for cardiac gating. The periodic inflow of blood is clearly reflected in the resulting DC signal (Figure 17), which is also slightly modulated by respiratory motion. To minimize lung motion, a gating window is set to expiration and only the cardiac cycles within this gating window are accepted. Later, different cardiac phases are defined by another gating window, shifted between the signal peaks (Figure 17 (c and d)).

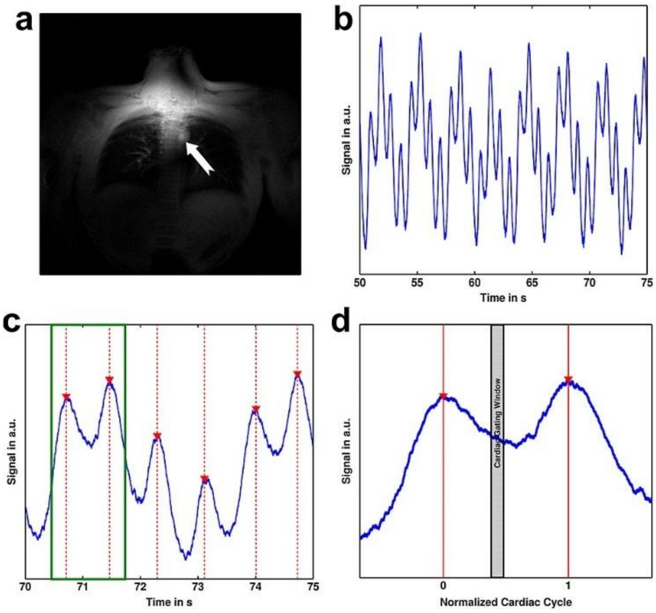

Figure 17. DC signal (b) measured with a coil element sensible to the cardiac motion (a). A gating window is shifted between peaks to segment the acquired data into different cardiac cycles. From Ref. [22], used with permission from John Wiley and Sons.

After reconstructing each dataset, a complete representative respiratory and cardiac cycle is obtained (Figure 18).

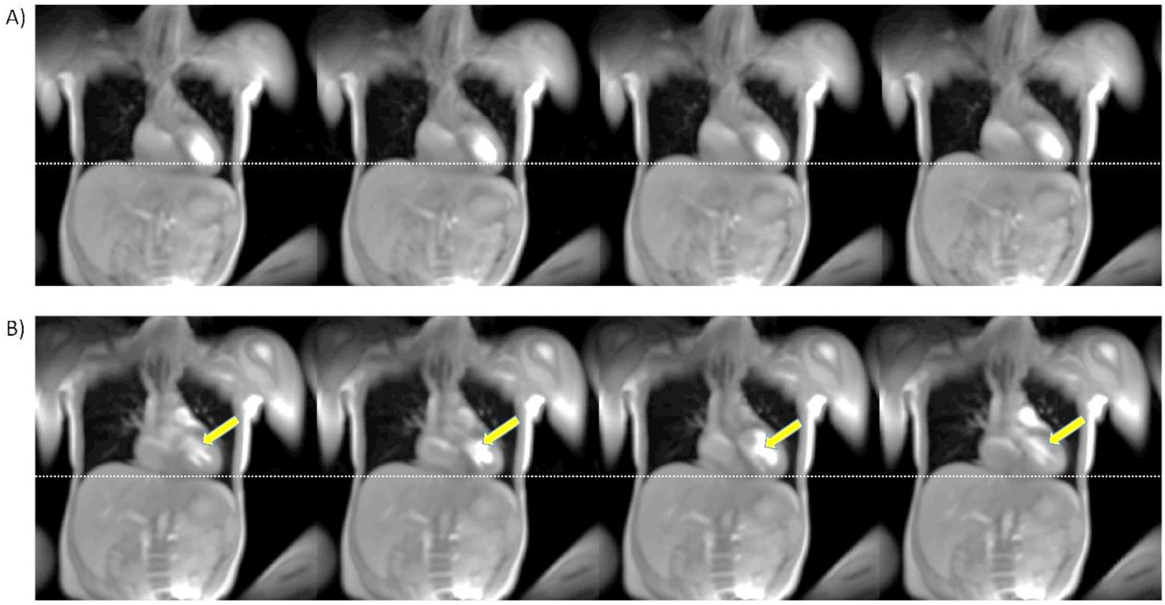

Figure 18. Four different respiratory (A) and cardiac (B) phases measured from a healthy subject, in free breathing, with SENCEFUL.

As displayed in Figure 18(A), the shape of the lungs changes significantly during a respiratory cycle, and an image registration technique is required in order to analyze corresponding regions across the image stack. A 2D-motion registration is applied to the time series, aligning the reconstructed images to a reference image. As reported by Ref. [22] best results are obtained when the reference image is halfway between the inspiration and expiration phases. As all cardiac phases are in the same respiratory phase, no motion correction is required for the cardiac cycle.

When the echo time is short, it can be assumed that the MR signal variations in the lung parenchyma, during a breathing cycle, are caused by the gas exchange process. The quantitative weighted ventilation value (QV) is then a measure of this signal change and offers a representation of the ventilation in ml air added during inspiration per ml of lung parenchyma. The idea is well established and was initially introduced by Ref. [65]. In this paper, QV is called Total Ventilation (V_{abs}), which is calculated as:

$$V_{abs} = \frac{S_{exp} - S_{insp}}{S_{exp} - S_{noise}} \qquad \text{Equation 5}$$

S_{exp} is the signal in the end-expiration phase, S_{insp} is the signal in the end-inspiration phase, and S_{noise} is a measurement of the noise. As this is mainly a subtraction of the end-inspiration and end-expiration phases, signal variations caused by noise lead to false ventilation information.

SENCEFUL typically determines these signal variations in a different fashion than Ref. [65]. Thereby, the QV is calculated in the frequency domain, which reduces the noise dependence. For that, not only two breathing phases are used, but also all the others in between.

QV can also be compared to the Vital Capacity, measured in liters, from a conventional pulmonary function test. For that, the QV (ml air/ml lung parenchyma) needs to be multiplied by the total lung volume, which can be determined by a thoracic MRI scan [65]. In general terms, it can be said that the QV offers a method to measure the Vital Capacity regionally.

Similar to FD-MRI, SENSEFUL extracts the function information after applying a pixel-wise Fourier transform. The functional contrast, for ventilation and perfusion, is observed in the real part of the spectral image from the lowest non-zero frequency component of the spectrum. The normalized signal amplitude from each pixel is then used to generate ventilation and perfusion-weighted maps.

Because of the Fourier transform approach, non-oscillating signals are not visualized in the functional maps. Additionally, through-plane motion and partial volume effects are still reported [66].

As a result of not being limited by a specific acquisition rate, SENCEFUL was able to acquire images with higher SNR and spatial resolution than FD-MRI [22].

SENCEFUL was already validated against Fourier decomposition and dynamic contrast-enhanced MRI (DCE-MRI). Examples of ventilation and perfusion maps are presented in Figure 19.

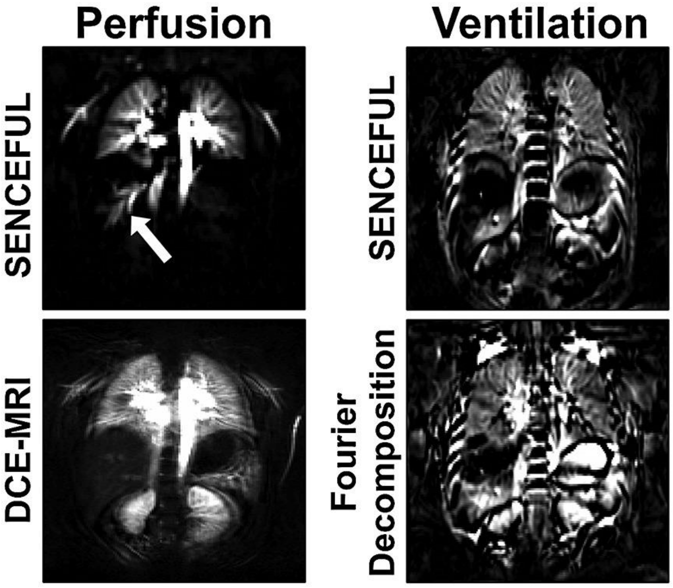
Perfusion
Ventilation
SENCEFUL
SENCEFUL
DCE-MRI
Fourier Decomposition

Figure *19*. Comparison of SENCEFUL with DCE-MRI and Fourier decomposition. For perfusion, SENCEFUL shows good accordance with the DCE-MRI data. For ventilation SENCEFUL and standard FD offer equivalent functional information. The SENCEFUL maps exhibit better visibility of the lung boundary, fewer artifacts, higher signal-to-noise ratio (SNR) and higher contrast than standard FD. From Ref. [22], used with permission from John Wiley and Sons.

SENCEFUL also presented good correlation with vital capacity tests when used to quantify the ventilation in patients with cystic fibrosis [66].

3 Methods

This work presents a method to assess lung ventilation in 3D by combining Self-gated Non-Contrast-enhanced Functional Lung MRI (SENCEFUL) with an ultra-short echo time (UTE) acquisition and a 3D image registration technique.

Six healthy volunteers (4 men, 2 women; mean age ± SD, 26 ± 2.0; range, 23 –29 years) and one patient with lung cancer (male, 62 years old) were included in the study. The patient had a non-small cell lung cancer in segment 3 of the left upper lobe and accumulated mucus in different regions of the lung.

All measurements were performed at the University Hospital of Würzburg, on a 3 Tesla MAGNETOM Prisma (Siemens Healthineers, Erlangen, Germany). Post-processing and reconstruction were conducted off-scanner on MATLAB®.

This project was approved by an institutional ethics committee and performed in accordance with the ethical standards as laid out in the 1964 Declaration of Helsinki and its later amendments. Informed consent was obtained from the participant prior to the study.

Ventilation weighted maps were generated and the quantitative ventilation values were assessed. Lung ventilation and image quality were compared between the new UTE-SENCEFUL and the standard 2D-SENCEFUL methods. Additionally, different gating techniques, reconstruction methods, and image registration processes were evaluated for UTE-SENCEFUL.

A description of the acquisitions, reconstructions, gating techniques and quantification of ventilation is presented in the following sub-chapters and can also be found in Ref. [62]. Excerpts and images of this paper were reproduced in this thesis, with permission from John Wiley and Sons.

3.1 3D-SENCEFUL

3.1.1 3D-UTE sequence and protocol

Initially, a 3D-UTE pulse sequence, with a radial center-out acquisition, was developed in the IDEA software environment, provided by Siemens Healthineers. The sequence consisted of a nonselective RF pulse excitation, followed by a 3D center out (koosh ball) acquisition. An illustration of the koosh ball trajectory and the sequence diagram is presented in Figure 20.

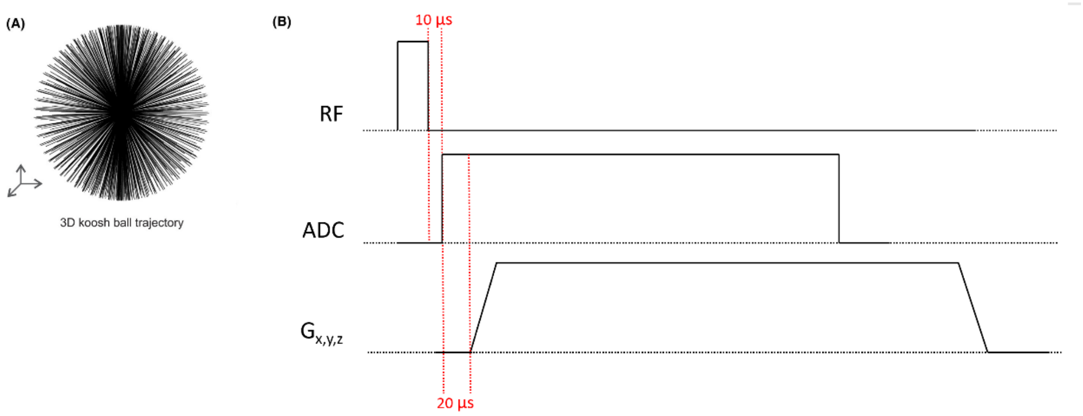

Figure 20. K-space trajectory and acquisition scheme. A) 3D koosh ball trajectory, filled in a quasi-random order. The center of the k-space is denser than its extremities. B) Sequence diagram, with the ADC starting 10 μs after the end of the RF pulse. The read-out gradients started 30 μs after the end of the RF pulse.

In order to achieve the shortest possible echo time, the k-space was also sampled while the gradients were ramping up. Considering the scanner dead time between the end of the RF pulse and the ADC, and the transient phase of the digital filter, an echo time of 30 μs was used in this application. The first readout points were acquired immediately after the transient phase of the digital filter.

The following acquisition parameters were applied during measurement:

Parameter	Value
TE (ms)	0.03
TR (ms)	1.78
Flip Angle	2 °
Resolution (mm^3)	2.3
FOV (mm^3)	300
Number of Projection	350000
Bandwidth (Hz/pixels)	2298
Matrix size	128x128x128
Total measurement time (min)	10.4

Table 1 – 3D-UTE measurement parameters

All examinations were performed using a body-coil array coupled on a 3 Tesla whole-body MR scanner (Siemens MAGNETOM Prisma; Siemens Healthineers, Erlangen, Germany) with maximum gradient amplitude of 80 mT/m and a maximum slew rate 200 T/m/s. The subjects were scanned in free breathing and head-first supine position.

3.1.2 DC gating

Because each projection starts in the center of the k-space, the average signal value of the first points acquired during readout can be used as the DC signal. In this experiment, the average value of the first five points after the transient phase of the DC signal was used. The DC signal was then filtered using a Savitzky-Golay function with a trinomial polynomial order and frame size of 801 points.

Next, the gating signal was extracted using two different approaches: a manual approach and an automatic method employing coil clustering [67]. For the first method, the DC signal from each individual coil was plotted and a single coil which presented high signal correlation with the breathing motion, was manually selected.

The second method, initially proposed by Ref. [67], combines the signal from a subset of coils elements that are highly correlated, to automatically determine the dominant motion. To this end, a correlation matrix of the DC signal from all coils was calculated. Next, a thresholding operation was applied to the correlation matrix, and all values above 0.95 were set to 1. Values smaller than the threshold were set to zero.

Principal component analysis was applied to calculate the eigenvalue decomposition of this matrix. To find the coil cluster, another thresholding operation was exploited. The coil cluster was selected based on the eigenvalues corresponding to eigenvectors higher than 0.4. The limits for both thresholding operations were empirically determined. A demonstration of the coil clustering algorithm is found in Figure 21.

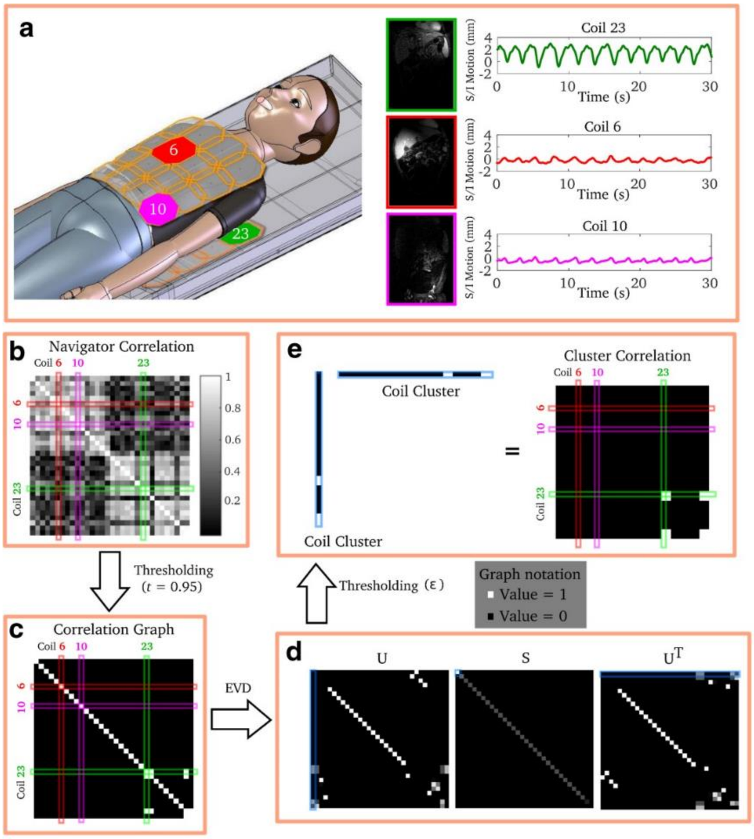
a
Coil 23
S/I Motion (mm)
Time (s)
Coil 6
Coil 10
6
10
23
b
Navigator Correlation
Coil 6 10 23
Thresholding
(t = 0.95)
c
Correlation Graph
EVD
d
U
S
U^T
e
Coil Cluster
Cluster Correlation
Thresholding (ε)
Graph notation
▫ Value = 1
▪ Value = 0

Figure 21. Coil clustering algorithm. (a) Navigators from three individual coil elements. (b) calculation of the correlation matrix; (c) construction of a correlation graph by thresholding the correlation matrix; (d) eigenvalue decomposition of the correlation graph; (e) thresholding of the eigenvector corresponding to the largest eigenvalue. Modified from Ref. [67], used with permission from John Wiley and Sons.

In this method for motion estimation, coils with negative correlation can also be present. Therefore, the signals from the coil cluster need to be aligned based on the sign of the correlation coefficient, so that they do not cancel out each other. The motion estimate was then calculated as the average DC signal within the coil cluster.

For comparison, time-resolved images and functional maps of three healthy subjects were also reconstructed using the DC signal from a single coil, which was manually chosen. The maximum of the first derivative in the lung-liver interface was used to calculate the distance in pixels, from the diaphragm in the end-inspiration and end-expiration phases. This distance was used as a quantitative parameter to compare the manual and automatic methods for DC gating and coil selection.

3.1.3 Data binning

The gating signals, obtained with the automatic and manual methods, offer a representation of the breathing motion. Thus, its signal variation can be used as a navigator to track the diaphragm position over time, such that the interval between the minimum and maximum signal amplitudes can be divided into individual time-frames.

The DC signal amplitude difference was normalized to one and eight gating windows were defined. Each window represented a different state of motion during a breathing cycle. The window width was defined such that each breathing phase had at least 50 thousand projections, which represents a sampling density of approximately 25% of the Nyquist sampling rate at k_{max}.

An illustration of the gating process is shown in Figure 22.

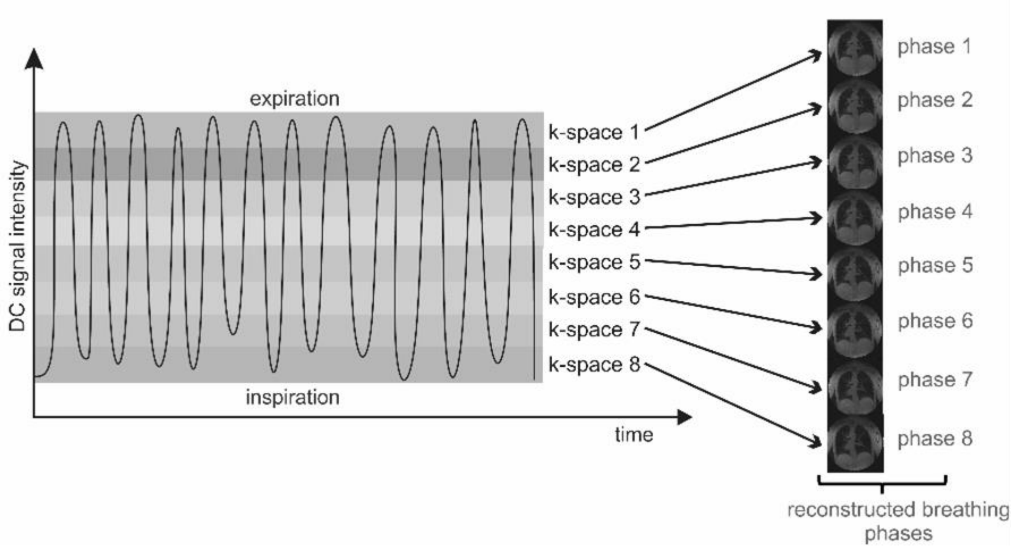
expiration
DC signal intensity
inspiration
time
k-space 1
k-space 2
k-space 3
k-space 4
k-space 5
k-space 6
k-space 7
k-space 8
phase 1
phase 2
phase 3
phase 4
phase 5
phase 6
phase 7
phase 8
reconstructed breathing phases

Figure 22. Gating process illustration. The filtered DC signal extracted from the k-space center, that is, the first readout points of each projection. The DC signal is used as a reference to segment the acquired raw data into 8 different k-spaces. After reconstruction, each k-space represents an individual breathing phase. Modified from Ref. [62], used with permission from John Wiley and Sons.

As presented earlier, 350000 spokes were acquired for each measurement. Hence, overlapping of the breathing phases occurred, and some spokes were assigned to 2 different phases.

The k-spaces, corresponding to each gating window, were individually reconstructed, as described next.

3.1.4 Trajectory correction and image reconstruction

After measurement, gradient errors were corrected in postprocessing using the Gradient Impulse Response Function (GIRF) approach [68,69]. GIRF completely characterizes the gradient system as a linear and time-invariant system, and it was used to correct deviated trajectories from 3D ultrashort echo time acquisitions [68,69]. The corrections were applied for all three axis and all coil channels.

Because the k-space related to each breathing phase is extremely undersampled, iterative SENSE was the method of choice to reconstruct the datasets [70].

SENSE-reconstruction unfolds by solving a set of linear equations to determine the “true” pixel values in the desired image, based on the sensitivities of the individual coil elements and the superposition of pixel intensities.

The reconstruction code was written based on the Michigan Image Reconstruction Toolbox (MIRT), which is an open source algorithm for image reconstruction on MATLAB® [71]. Using MIRT, low-resolution images were reconstructed from each surface coil and the complex sensitivity profiles of each coil element was calculated.

For comparison, the ungated dataset from a single subject was reconstructed with SENSE, and also re-grid in a Cartesian fashion and reconstructed using a Fast Fourier Transformation (FFT).

All reconstructions were performed off-scanner, on a workstation with 64 CPU cores and 256 GB of RAM.

3.1.5 Ventilation quantification

In order to asssess the signal variation caused by respiration, the respiratory motion needs to be suppressed and the lung structures must be aligned in the image stack. For this purpose, a demon-based nonrigid 3D image registration technique was employed [72]. All breathing phases were registered to one intermediate phase, with approximately the same extent of deformation with respect to inspiration and expiration.

Next, a symmetric Hamming filter, with a window width of 1.25 times the k-space matrix size and a maximum signal amplitude of 1, was used to smooth the images before the generation of the ventilation maps.

To take advantage of all reconstructed breathing phases and minimize the contribution of noise, a model function was fitted to the signal evolution over the breathing cycle. A simple shifted sine curve model with offset was assumed. According to this model, the signal of the first harmonic in the frequency domain is half the signal amplitude of the sine wave in the time domain. The Quantitative weighted Ventilation value (ml of gas/ ml of lung tissue) was evaluated as two times the amplitude of the first harmonic in the frequency domain, normalized by the signal in expiration.

After quantifying the ventilation on each voxel, the lungs were manually masked in different regions and the mean Quantitative weighted Ventilation value ± standard deviation for each lung area was calculated for all volunteers. The signal intensities assigned to the blood vessels were manually set to zero using a simple threshold approach, before generating the functional maps.

An illustration of the different lung regions for regional ventilation assessment is shown in Figure 23.

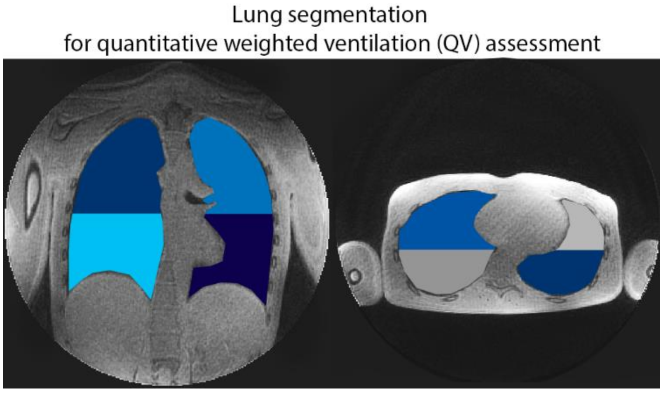

Figure 23. Lung segmentation. The lungs were divided into the following regions: total lung; right lung; right lung: upper half; right lung: lower half; left lung; left lung: upper half; left lung: lower half. Additional regions were analyzed only for the 3D-UTE measurement, including the right lung: posterior half; right lung: anterior half; left lung: posterior half; and left lung: anterior half. QV, quantitative weighted ventilation. Image from Ref. [62], used with permission from John Wiley and Sons.

Additionally, to show the benefits of the 3D image registration and to estimate the influence of through-plane motion in the ventilation maps, a 2D registration method was applied to each partition of the nonregistered 3D data set from a healthy volunteer. Ventilation weighted maps were generated and the level of artifacts in the functional maps was compared to the 3D image registration technique.

3.2 2D-SENCEFUL

In addition to the 3D-UTE measurement, 2D-SENCEFUL measurements were conducted with a modified FLASH sequence with a quasi-random ordering of the phase encoding. For the gating process, the DC signal was acquired for 20 µs, 250 µs after completion of the readout. The acquisition diagram is presented in Figure 24.

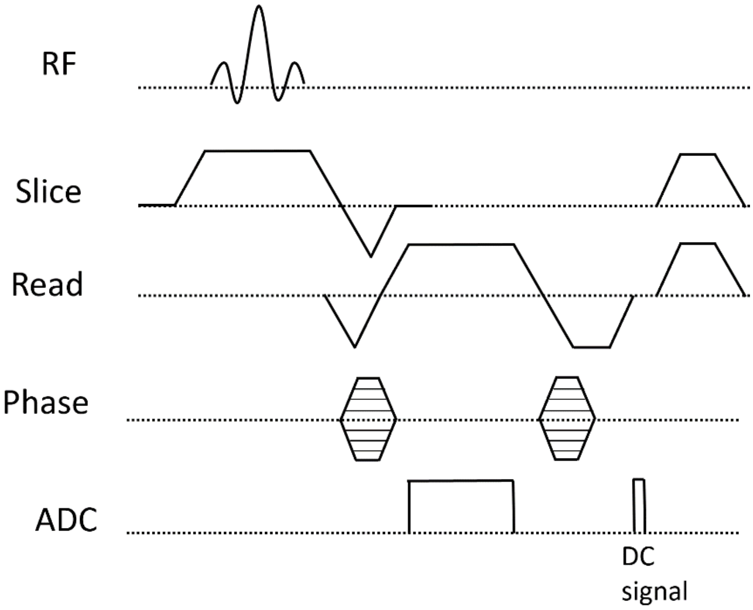

Figure 24. Fast low-angle shot sequence diagram, with additional sampling of the direct current (DC) signal.

For each subject, six adjacent coronal slices covering the midcoronal region were measured. The following measurement parameters were used:

Parameter	Value
TE (ms)	0.7
TR (ms)	2.5
Flip Angle	8 °
Resolution (mm^2)	4.5
FOV (mm^2)	350
Slice thickness (mm)	10
Repetitions	500
Total measurement time (min)	2.7

Table 2. 2D-FLASH acquisition parameters.

The DC signal from a coil element close to the diaphragm, and with high signal correlation with the respiratory motion, was used for gating. The signal was filtered using a Savitzky–Golay function with a trinomial polynomial order, and frame size of 301 points.

The DC signal amplitude was normalized to one, and eight individual k-spaces—each representing a breathing phase—were sorted. A simple inverse Fourier Transform was applied to convert the data to the image domain.

All breathing phases were registered into an intermediate phase using a 2D nonrigid image registration with a free-form deformation based on B-splines [73]. The target breathing state presented a similar extent of deformation with respect to the end-inspiration and end-expiration phases.

Prior to the generation of the functional information, a 2D Hamming window with the maximum signal amplitude of 1 and window width of 1.25 times the k-space matrix size was used as a filter to denoise the reconstructed images.

Each coronal slice was manually masked in different regions and the average ventilation for each location was calculated. Because the number of measured slices with 2D-SENCEFUL was not enough to cover the whole lung, the ventilation for the anterior and posterior halves of the lung was not assessed.

The images acquired using the 2D-FLASH and 3D-UTE techniques were compared regarding their image quality and quantitative ventilation values. Their corresponding functional maps and morphological images were set side by side with respect to recognition of the lung structures, artifact level and clinical quality of the ventilation information. The mean QV values were also compared among the two acquisition techniques and the literature.

3.3 SNR comparison

The noise behavior in the 3D-UTE and 2D-FLASH acquisition was compared using the pseudo multiple replica method [74]. This approach employs a Monte Carlo simulation to create artificial noise, based on a single noise measurement. The noise measurement is used to determine the noise correlation among different coil channels and to produce authentic artificial noise.

For that, noise scans were performed in a healthy subject with the RF voltage set to zero, for both the 2D and 3D methods. The subject was measured in tidal breathing and using the same setup, MR protocol, and coil configuration as for the diagnostic acquisitions. An additional diagnostic measurement was also performed.

A hundred noise-only datasets were created for the 2D-FLASH acquisition, and fifty different datasets were created for the 3D-UTE. The noise datasets were scaled by a factor of 0.1 and added to the k-space from the diagnostic measurements.

The 3D-UTE datasets were reconstructed with SENSE and an inverse Fourier transform was employed in the 2D-FLASH reconstruction.

After reconstruction of each dataset, the SNR was calculated for every pixel along the stack of images of the 2 different acquisition, as the mean signal intensity was divided by 10 times its standard deviation.

The lungs were then segmented and the mean SNR value for the coronal slice in the lung was determined for the 2D-FLASH and 3D-UTE measurements.

4 Results

4.1 Non-gated reconstruction

The SENSE reconstruction has improved the overall image quality of the measured data. In Figure 25 (A), the image was reconstructed with an inverse fast Fourier Transform, after the non-Cartesian data was resampled into a Cartesian grid. The same data, reconstructed with SENSE, is presented in Figure 25 (B). The measurement was performed in tidal breathing and no gating technique was applied.

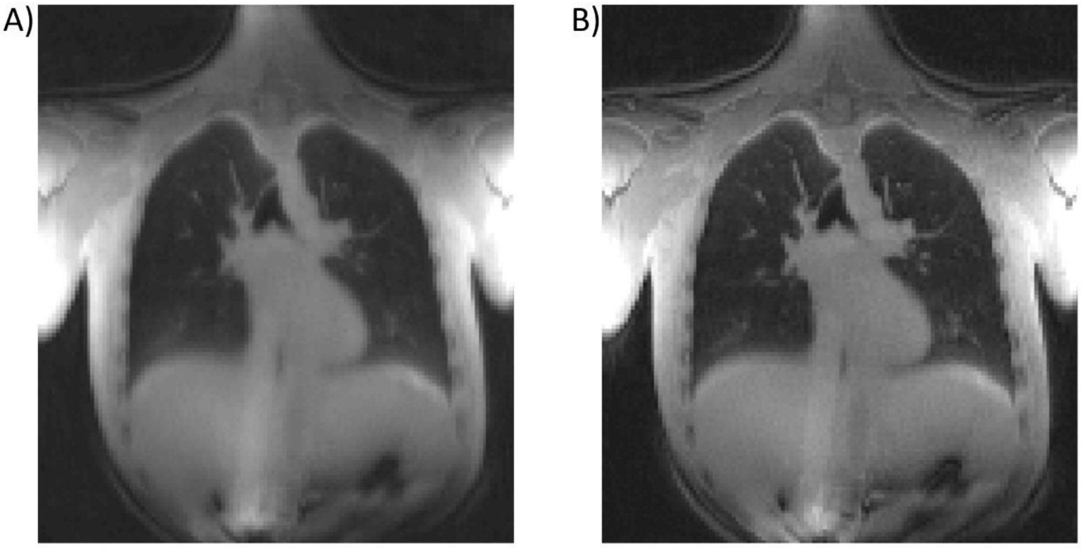

Figure 25. Comparison between SENSE and traditional gridding. In A) the k-space was re-grid in a 3D cartesian grid and reconstructed with an invest Fourier Transform. B) presents the same dataset reconstructed with SENSE.

SENSE has drastically improved the overall image quality, with less blurring and improved SNR. Receive coil inhomogeneity was also reduced. Nevertheless, the reconstruction time was considerably longer. For a rawdata with 50000 radial projections, the traditional gridding process takes one hour and twenty minutes. For the same dataset, SENSE took four hours and fifteen minutes to reconstruct the data.

4.2 Self-gating and morphological images

4.2.1 Coil clustering versus manual selection

The DC signal measured with the 3D-UTE acquisition and extracted from the k-space center provided consistent respiratory motion estimation for all subjects. An example of a gating signal, measured from a healthy volunteer, is presented in Figure 26.

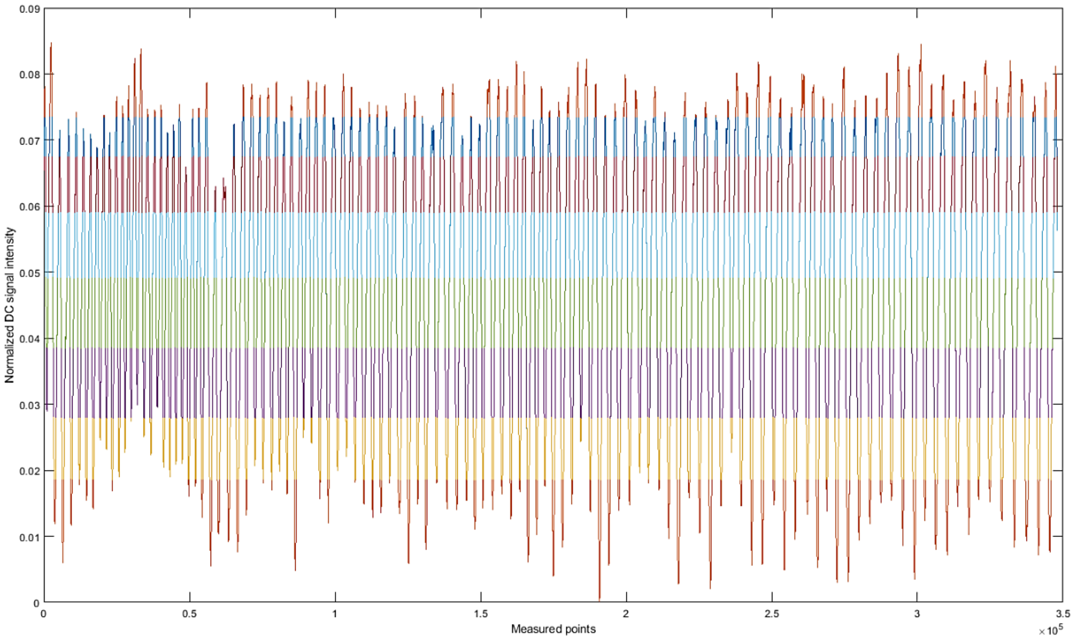

Figure 26. Filtered DC signal extracted with the coil clustering algorithm. The different colors represent the gating windows.

Coil clustering and manual selection of the DC signal were both reliable and presented very good correlation, as seen in Figure 27.

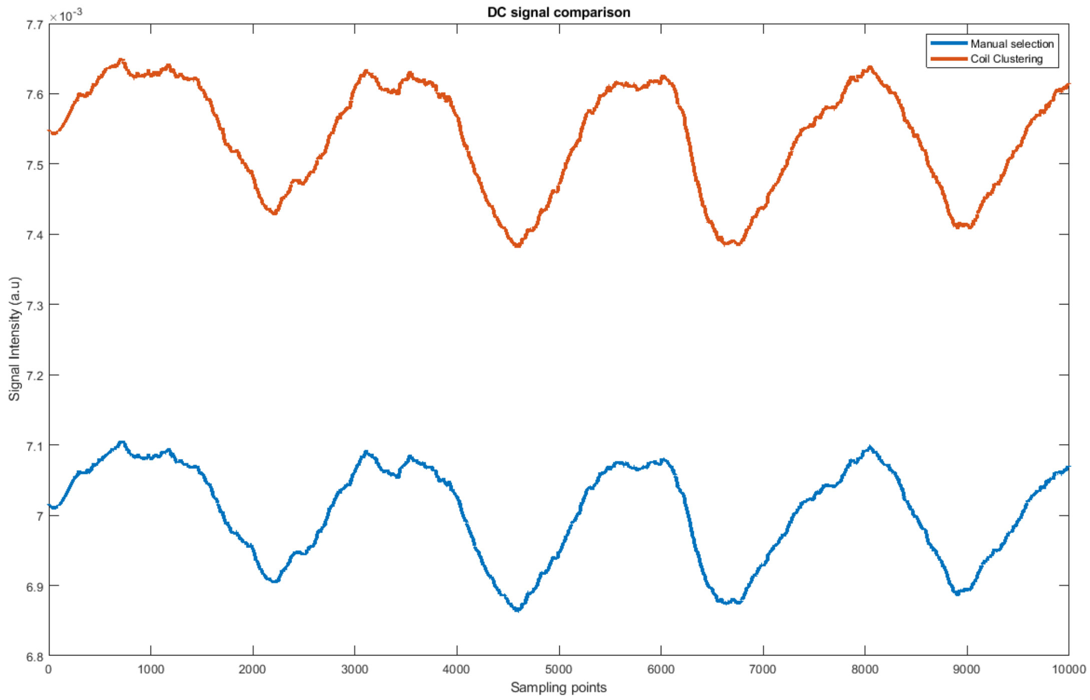

Figure 27. DC signal from a manually chosen coil compared to the DC signal from a coil-cluster.

After reconstruction, image sharpness was visually similar in both gating techniques. The distance between the lung-liver interface in the end-inspiration and end-expiration phases was, on average, 7% larger in images reconstructed using the coil-clustering method. An end-inspiration and end-expiration breathing phases, reconstructed using coil clustering and a manually selected DC signal from a single coil element are shown in Figure 28.

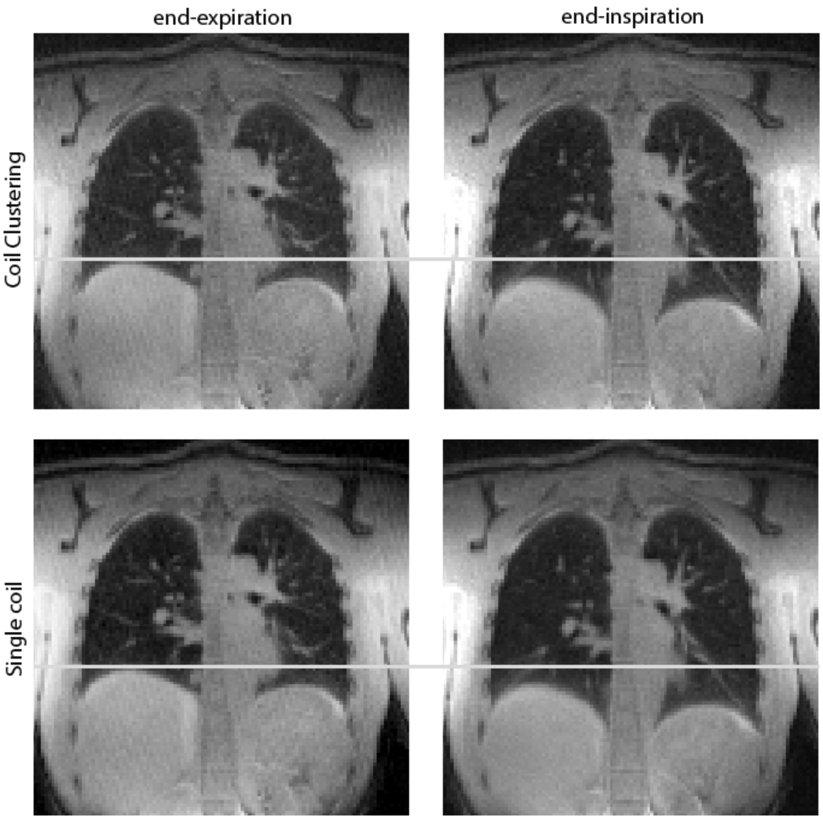

Figure 28. Comparison of coil clustering and manual selection of the DC signal. End-inspiration and end-expiration breathing phases reconstructed using a coil clustering algorithm for DC-gating and a manually selected DC signal from a single coil element. In this figure, only the coronal slice from a reconstructed breathing phase is presented. SENSE was used to determine the fully sampled data.

Coil clustering was also a reliable form of gating for the patient with lung cancer. The patient was very debilitated, with irregular breathing motion, especially during the first half of the measurement. Such irregularities were properly reflected in the DC signal, as highlighted by the dashed rectangles in Figure 29.

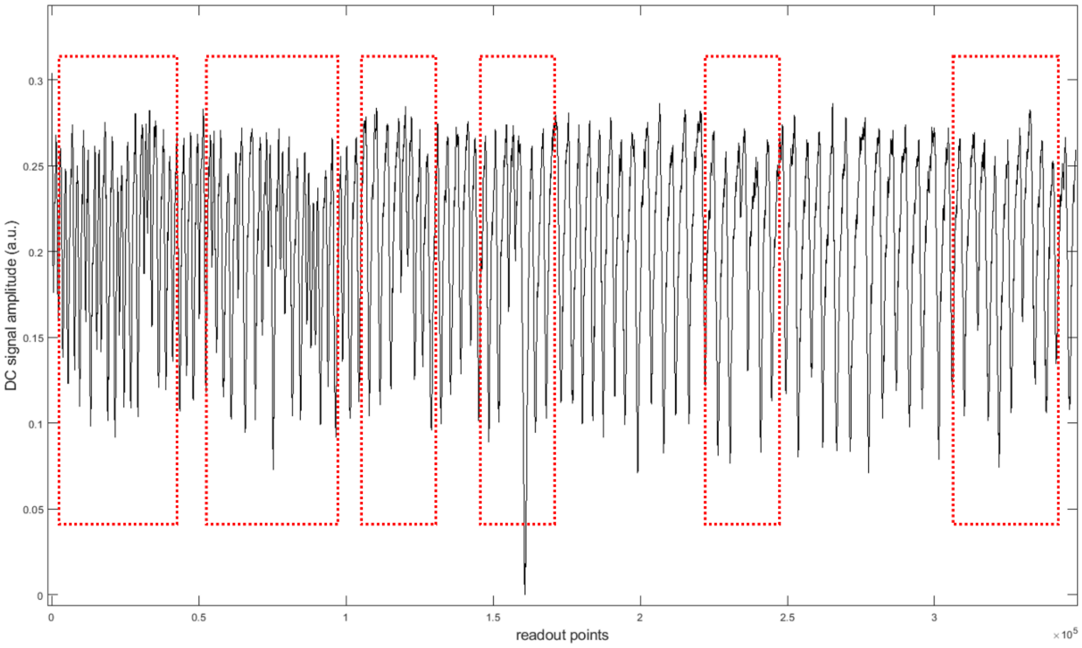

Figure 29. Gating signal from a patient with lung cancer. The signal was calculated with a coil clustering algorithm. The patient was debilitated and presented irregular motion during measurement. The effect of this irregularity was reflected in the DC signal. Areas of instability are highlighted with the dashed rectangles.

4.2.2 3D-UTE versus 2D-FLASH

Figure 30 shows four breathing phases reconstructed from a healthy volunteer using the 3D-UTE and 2D-FLASH acquisitions. For both techniques, the different breathing states and corresponding positions of the diaphragm during a breathing cycle can be clearly delineated.

The improved SNR and increased spatial resolution of the 3D-UTE allowed for a better visualization of parenchyma and blood vessels, which were only slightly visible with the 2D measurement.

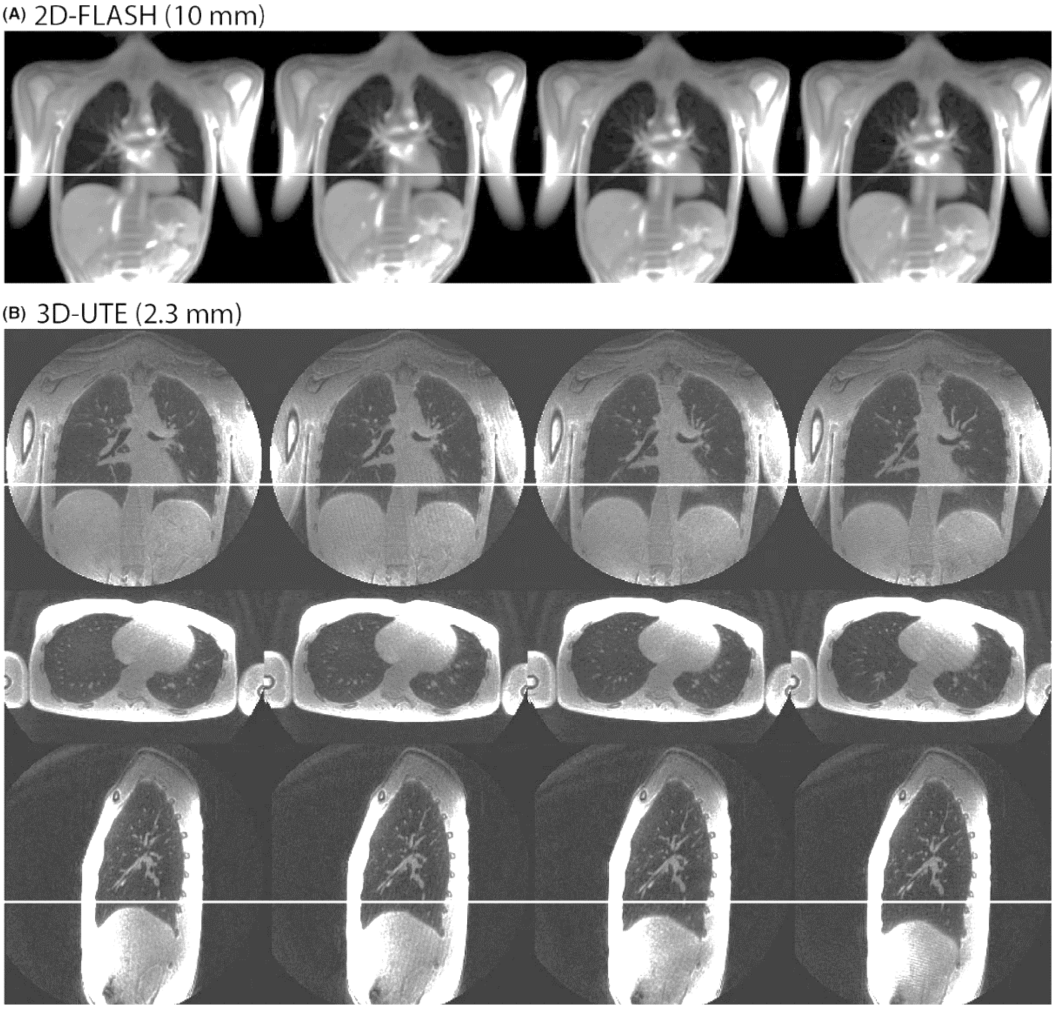

Figure 30. Four reconstructed breathing phases from a healthy volunteer, using 2D-FLASH and 3D-UTE. The 2D-FLASH images (A) were reconstructed from a single measurement, with a scanning time of 2.7 min. To cover the whole lung, usually more than 12 slices are required (depending on the volunteer), which can take more than 32 min. The presented 3D-UTE images (B) were sections extracted from the 3D reconstruction, with a total measurement time of 8.7 min. With a shorter TE and TR and higher SNR, 3D-UTE was able to improve the resolution and finely depict the lung structures, which were not visible in the 2D-FLASH acquisition. Image from Ref. [62], used with permission from John Wiley and Sons.

The mean SNR in the lung for the UTE acquisition was 49% larger than the SNR measured with the 2D-FLASH. SNR maps, measured from a healthy, are seen in Figure 31.

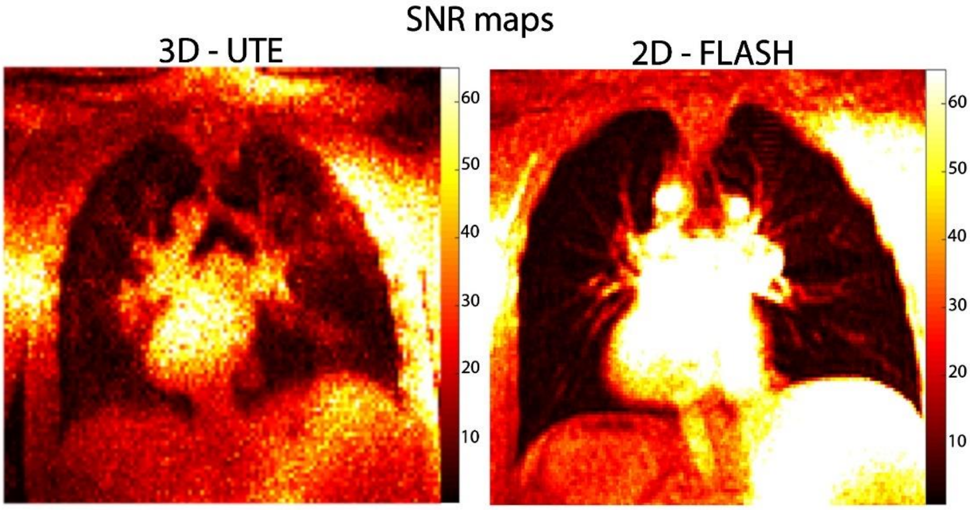
SNR maps
3D - UTE
2D - FLASH
60
50
40
30
20
10
60
50
40
30
20
10

Figure 31. SNR maps from similar coronal slices, measured from a healthy subject, is presented for the 2D-FLASH and 3D-UTE acquisitions. The mean SNR in the lung was found to be 49% higher for the UTE measurement, compared to the 2D FLASH acquisition with a low spatial resolution. Image from Ref. [62], used with permission from John Wiley and Sons.

4.3 Ventilation assessment and quantification

UTE-SENSEFUL was able to successfully assess the ventilation for all healthy subjects and the patient with lung impairments. The results, which are shown in this sub-chapter, were also published in Ref. [62] and are reproduced here with permission from John Wiley and Sons.

4.3.1 2D image registration versus 3D image registration

A coronal view of the end-inspiration and end-expiration breathing phases after 3D and 2D image registration is displayed in Figure 32. The corresponding unsegmented ventilation-weighted map is also seen for both registration methods.

As observed, the 2D image registration is not able to account for through-plane motion, which results in signal changes across the image stack that mimic the signal variation caused by the respiratory process. Such artifacts, as pointed by the yellow arrows, led to false ventilation information.

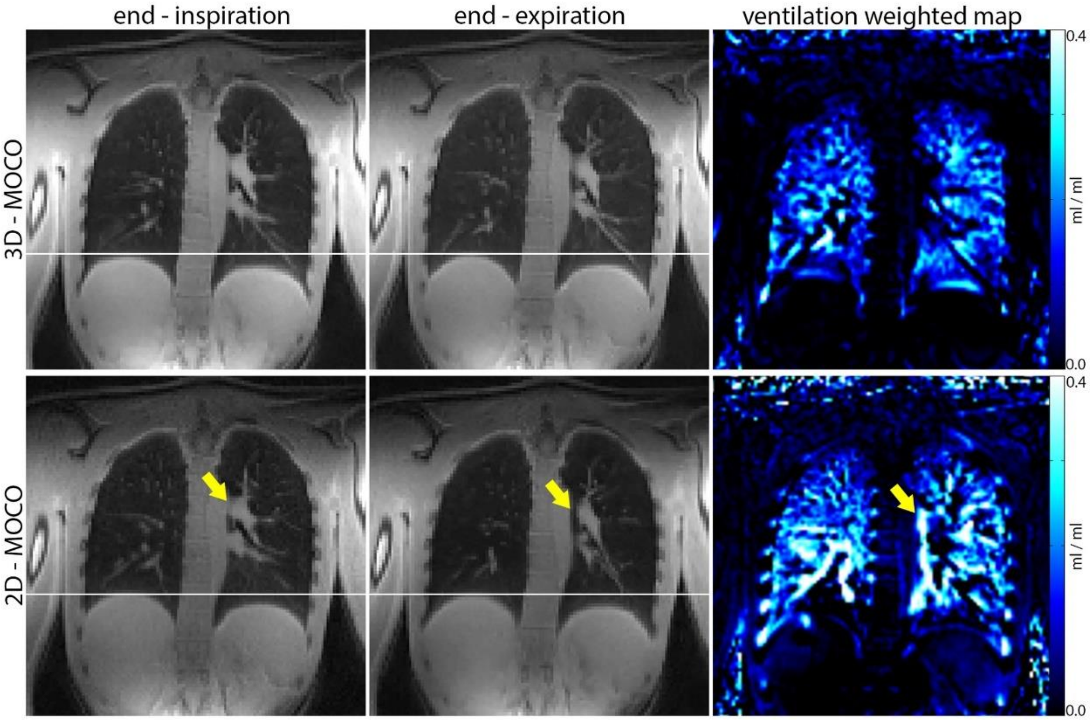
end - inspiration
end - expiration
ventilation weighted map
3D - MOCO
2D - MOCO
0.4
0.0
ml / ml

Figure 32. 2D and 3D image registration comparison. Exemplary results of the UTE-SENCEFUL in a healthy volunteer, depicting the end-inspiration and end-expiration breathing phases subsequently to 3D and 2D image registration. The corresponding ventilation-weighted maps are presented in the right column. As pointed by the yellow arrows, the 2D image registration technique is less robust against through-plane motion, resulting in ventilation artifacts. Image from Ref. [62], used with permission from John Wiley and Sons.

The 3D motion correction still struggled in regions with a lot of motion, especially in the diaphragm. However, the number of ventilation artifacts was considerably reduced when compared to the 2D method.

4.3.2 Ventilation assessment and quantification in the control group

Figure 33 presents one breathing phase in the coronal, axial, and sagittal planes after 3D image registration, as well as the corresponding ventilation-weighted maps generated by UTE-SENCEFUL for a healthy volunteer. Moreover, the ventilation-weighted map generated with the conventional 2D-SENCEFUL and the corresponding morphological image after 2D image registration are displayed for comparison.

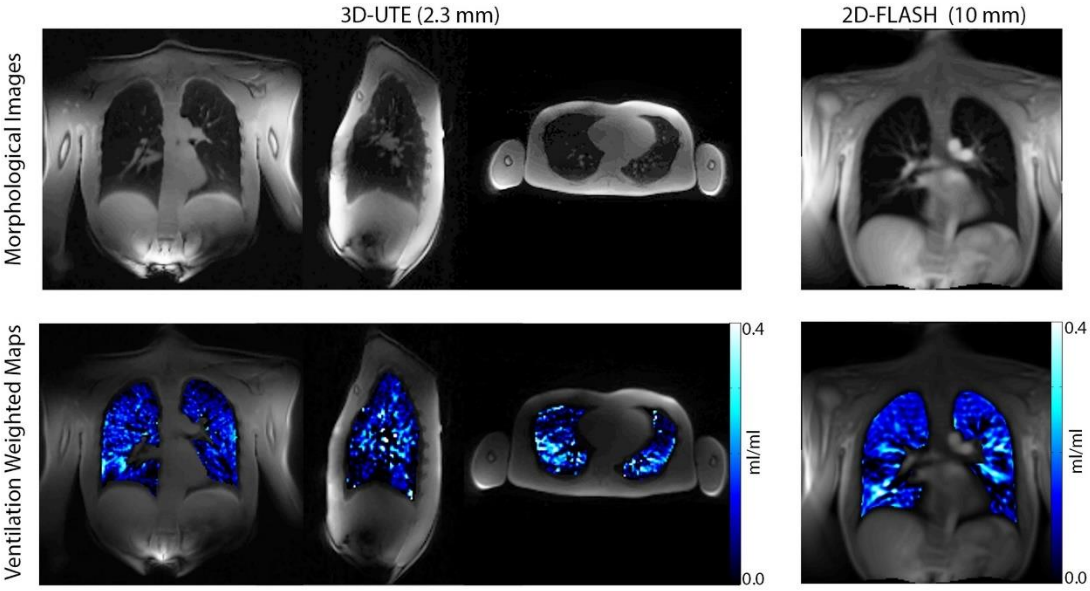
3D-UTE (2.3 mm)
2D-FLASH (10 mm)
Morphological Images
Ventilation Weighted Maps
0.4
ml/ml
0.0
0.4
ml/ml
0.0

Figure 33. Ventilation-weighted maps from a healthy subject. 3D morphological images after image registration and ventilation-weighted maps using UTE-SENCEFUL and the standard 2D-SENCEFUL approaches. UTE-SENCEFUL ventilation maps have a slice thickness of 2.3 mm, compared to 10 mm for the 2D-SENCEFUL. In the right column, the faint ventilation artifacts in the upper part of the lungs were introduced by the 2D image registration. Image from Ref. [62], used with permission from John Wiley and Sons.

In Figure 33, no indication of impairment is found in the structural or functional images. The same applies to the other measured healthy volunteers, which is confirmed by the quantitative ventilation values presented in Table 1.

Lung Region	2D-SENCEFUL (ml/ml)			UTE-SENCEFUL (ml/ml)			Mann-Whitney test (p=0.05)
	M	SD	MDN	M	SD	MDN	
Total lung	0.11	0.07	0.11	0.11	0.08	0.10	Not different
Right lung	0.11	0.07	0.10	0.11	0.08	0.10	Not different
Right lung - upper half	0.11	0.06	0.11	0.10	0.08	0.09	Not different
Right lung - lower half	0.11	0.08	0.10	0.11	0.09	0.11	Different
Right lung - posterior half				0.12	0.09	0.10	
Right lung - anterior half				0.10	0.08	0.11	
Left lung	0.11	0.08	0.11	0.11	0.08	0.10	Not different
Left lung - upper half	0.11	0.06	0.11	0.10	0.07	0.09	Not different
Left lung - lower half	0.11	0.09	0.12	0.12	0.09	0.11	Not different
Left lung - posterior half				0.12	0.09	0.10	
Left lung - anterior half				0.11	0.08	0.10	

Table 3. Average quantitative weighted ventilation values from the group of healthy subjects, assessed with UTE-SENCEFUL and 2D-SENCEFUL. UTE-SENCEFUL values are the average QV of the whole specified lung region and the 2D-SENCEFUL values are the average QV of six different coronal slices. The results of the statistical test, comparing the two methods, are presented in the last column. The average values of 2D-SENCEFUL and UTE-SENCEFUL were only statistically different in the lower half of the right lung. Abbreviations: M, mean; SD, standard deviation; MDN, median. Table from Ref. [62], used with permission from John Wiley and Sons.

The average quantitative ventilation values among all healthy volunteers for both UTE-SENCEFUL and 2D-SENCEFUL were 0.11 ± 0.08 mL/mL and 0.11 ± 0.07 mL/mL, respectively.

Mann-Whitney test examination has confirmed, within a 95% confidence level, that the average QV values were only significantly different, between UTE and FLASH, in the lower half of the right lung.

In UTE-SENCEFUL, ventilation in the posterior halves of the lung was higher than in the anterior halves, which reflected the gravitational effect [61]. Other smaller changes among different regions were only visualized by UTE-SENCEFUL.

4.3.1 Ventilation assessment and quantification in a patient

In Figure 34, morphological views and ventilation-weighted maps from the patient with lung impairments are presented. Sagittal, coronal, and axial views depict the ventilation deficit in the tumor area, which can be compared with the morphological images. The impact from the lung tumor was observed in the ventilation maps from both 2D-SENCEFUL and UTE-SENCEFUL, and other ventilation defects were found, especially in the posterior and lower halves of the right lung.

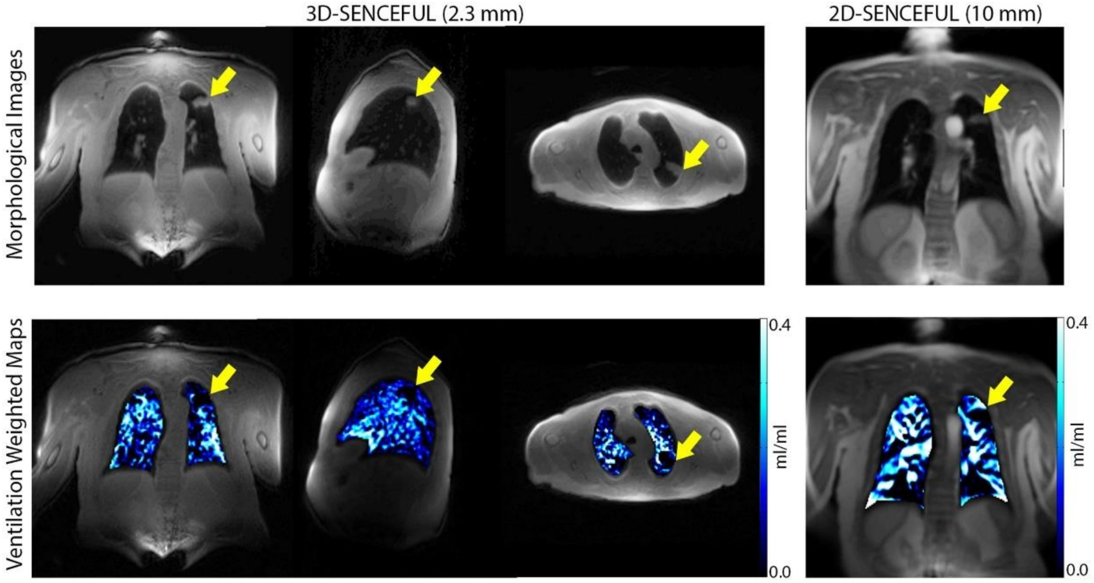

Figure 34. Ventilation-weighted maps from a patient with lung cancer. 3D morphological images after image registration and ventilation-weighted maps from a patient with a lung tumor using UTE-SENCEFUL and 2D-SENCEFUL. The patient suffered from accumulated mucus, and the lungs were inflated. The yellow arrows indicate the tumor area and its impact on lung ventilation. Other ventilation defects are observed in different parts of the lung. Image from Ref. [62], used with permission from John Wiley and Sons.

As visualized in images from the right column, 2D-SENCEFUL ventilation maps suffered from partial volume effects and through-plane motion. This problem was found in all measured slices and was even more evident in the QV values, which were unrealistically high for the standard technique, with higher values than the control group. For both 2D and UTE SENCEFUL, an overall increase in the SDs was observed compared to the healthy subjects. The average QV values for the whole lung ± SD for the patient scanned with UTE-SENCEFUL and 2D-SENCEFUL were 0.11 ± 0.10 mL/mL and 0.18 ± 0.17 mL/mL, respectively. Further details can be seen in Table 4.

Lung Region	2D-SENCEFUL (ml/ml)			UTE-SENCEFUL (ml/ml)		
	M	SD	MDN	M	SD	MDN
Total lung	0.18	0.17	0.16	0.11	0.10	0.09
Right lung	0.18	0.17	0.15	0.12	0.10	0.10
Right lung - upper half	0.20	0.17	0.20	0.11	0.10	0.09
Right lung - lower half	0.15	0.17	0.09	0.13	0.11	0.11
Right lung - posterior half				0.13	0.11	0.12
Right lung - anterior half				0.10	0.10	0.07
Left lung	0.19	0.16	0.18	0.10	0.09	0.08
Left lung - upper half	0.20	0.16	0.19	0.09	0.08	0.07
Left lung - lower half	0.19	0.16	0.18	0.11	0.09	0.10
Left lung - posterior half				0.09	0.09	0.08
Left lung - anterior half				0.10	0.09	0.08

Table 4. Quantitative weighted ventilation values assessed using UTE-SENCEFUL and 2D-SENCEFUL for a single patient with lung cancer. 2D-SENCEFUL values were unrealistically high, including in the upper part of the left lung, where the tumor is localized. A reduction in ventilation in the upper half of the left lung was depicted by UTE-SENCEFUL, which also presented an overall smaller standard deviation. Abbreviations: M, mean; SD, standard deviation; MDN, median. Table from Ref. [62], used with permission from John Wiley and Sons.

QV values assessed using UTE-SENCEFUL and 2D-SENCEFUL for a single patient with lung cancer. 2D-SENCEFUL values were unrealistically high, including in the upper part of the left lung where the tumor is localized. A reduction in ventilation in the upper half of the left lung was depicted by UTE-SENCEFUL, which also presented an overall smaller SD.

The impairment in the tumor area (left lung: upper half) was reflected by UTE-SENCEFUL. The upper half region of the left lung had an average ventilation 18%

lower than the lower half region of the left lung and the upper half region of the right lung. The ventilation in the left lung was also smaller than the right lung.

5 Discussion

SENSEFUL MRI exploits the direct current signal variations induced by the cardiac and breathing motion to generate functional contrast. For this purpose, representative breathing and cardiac cycles are created, and the ventilation and perfusion information is extracted in the frequency domain.

When compared to Fourier Decomposition, SENSEFUL has shown functional maps with higher SNR and temporal resolution. Additionally, SENCEFUL presented a solution for spectral broadening, by fitting the measured data into a model.

Notwithstanding the improved functional maps, the SNR in the structural images was still limited by long echo times and poor spatial resolution. Ventilation artifacts have also been reported, as consequence of the large slice thickness and residual motion after 2D image registration.

Aiming to solve the remaining problems, this study combined a 3D-UTE acquisition with SENSEFUL MRI. As direct benefits, 3D-UTE was able to reduce the echo time from 0.7 ms with 2D-FLASH to 0.03 ms with UTE. The slice thickness was greatly reduced, from 10 mm to 2.3 mm. However, the main benefit was the reduction in measurement time.

In 2D-SENSEFUL, the measurement time per slice is 2.7 minutes, and between eight and twelve slices are required to cover the whole lung, which can take up to thirty-two minutes. UTE-SENCEFUL was able to scan the whole lung in about ten minutes.

Concerning scanner noise, patient comfort was additionally improved with UTE. Because of the constant gradient switching, the 2D-FLASH acquisition is considerably louder, which might be a safety risk when proper hearing protection is not used [75].

Another benefit of the 3D-UTE is the intrinsic sampling of the k-space center with every readout. That allows for the omission of an additional measurement after each phase-encoding step, as it was previously necessary for the conventional 2D-SENCEFUL.

When manually selected, DC signals with high correlation with breathing motion were found for all measurements. Previously, the signal from a single coil was chosen for gating in 2D-SENSEFUL [22,66]. Aiming to create a more robust method for motion estimation, coil clustering for dense coil arrays was combined with a 3D radial acquisition in this work.

Coil clustering benefits have been demonstrated for cardiac and respiratory motion estimation with a cartesian acquisition [67]. For the 3D-UTE acquisition, coil clustering improved signal gating, which resulted in sharper reconstructions of the breathing phases. Because of the lack of perfusion information in 3D-UTE, the cardiac motion was not evaluated.

The impact of gating instabilities and non-uniform breathing patterns, like the one observed in the patient with lung impairment, were not evaluated in this work. Nevertheless, it is possible to assume that dubious gating can regrade the image quality, and future considerations in this aspect might be necessary for a more robust clinical implementation.

When compared to 2D-SENCEFUL, UTE-SENCEFUL radically improved the quality of the morphological images. Fine structures of the lung, which were not visible with FLASH, are now visible with UTE. This was mainly a result of the short echo time achieved with UTE, in combination with an appropriate reconstruction method.

The main constraints to a better image quality were the data size and measurement time. In order to achieve full Nyquist sampling rate, for each breathing phase, approximately 206 thousand spokes per breathing phase would have to be acquired.

The current setup, with a total number of 350 thousand projections, results in a rawdata file larger than 20 GB (depending on the number of coils selected). Therefore, increasing the number of radial acquisitions is not only impractical because of the increase in measurement time, but mainly because of the huge amount of data generated. An alternative approach would be to reconstruct fewer breathing phases, but this has not been investigated in this study.

UTE robustness against motion artifacts, as reported by Ref. [50,76], was confirmed by the findings of this thesis. When combined with a 3D image registration technique, the 3D-UTE acquisition reduced the number of ventilation artifacts in the functional maps, especially those caused by through-plane motion, which were a common cause of artifacts for 2D-SENCEFUL.

As observed in the 2D-SENCEFUL investigation of the patient with lung cancer, partial volume effects caused by a large slice thickness and residual signal changes caused by through-plane motion resulted in large areas of false ventilation and an unrealistic QV value. In this study, the patient was debilitated and presented intense and irregular breathing, which could not be accommodated by 2D-SENCEFUL. Due to better compliance, fewer artifacts were found in healthy subjects.

The lungs were manually segmented to calculate the regional ventilation. This process is time-consuming, particularly for three-dimensional datasets. Alternative approaches for automatic masking and segmentation are available and should be considered in the future.

In this work, the QV value for each lung region was calculated as the average value of the total number of pixels inside the segmented area. By doing so, the signal from areas with very low ventilation, in general in the outermost parts of the lung, were included in the measurement, which has increased the SD when compared to previously published data. Still, the mean values for the control group are in good agreement with Ref. [66], and the correlation of the QV with pulmonary function can be further analyzed in a clinical study.

When compared to 2D-SENCEFUL, UTE-SENCEFUL was able to improve the overall quality of the morphological and functional images while reducing total scan time. Concerning technical limitations, the 3D-UTE acquisition is not able to assess lung perfusion.

6 Conclusion

This work presented a self-gated method to evaluate pulmonary ventilation in three dimensions without the administration of contrast agents, by introducing a 3D-UTE in the SENCEFUL framework.

Pulmonary ventilation was successfully assessed and quantified using a three-dimensional ultrashort echo time sequence in SENCEFUL MRI for a group of healthy subjects and a patient with lung impairments.

When compared to the 2D approach, UTE-SENCEFUL has provided structural images with a better representation of the lung morphology, a 3D time-resolved reconstruction of the breathing cycle, and the possibility of assessing the ventilation in free-breathing for the whole lung with a single measurement.

UTE-SENCEFUL, combined with a 3D image registration technique, was also able to better account for through-plane motion and reduce ventilation artifacts in the functional maps.

7 Summary

In this thesis, a 3D Ultrashort echo time (3D-UTE) sequence was introduced in the Self-gated Non-Contrast-Enhanced Functional Lung Imaging (SENCEFUL) framework. The sequence was developed and implemented on a 3 Tesla MR scanner. The 3D-UTE technique consisted of a nonselective RF pulse followed by a koosh ball quasi-random sampling order of the k-space. Measurements in free-breathing and without contrast agent were performed in healthy subjects and a patient with lung cancer.

A gating technique, using a combination of different coils with high signal correlation, was evaluated in-vivo and compared with a manual approach of coil selection. The gating signal offered an estimation of the breathing motion during measurement and was used as a reference to segment the acquired data into different breathing phases.

Gradient delays and trajectory errors were corrected during post-processing using the Gradient Impulse Response Function. Iterative SENSE was then applied to determine the fully sampled data.

In order to eliminate signal changes caused by motion, a 3D image registration was employed, and the results were compared to a 2D image registration method.

Ventilation was assessed in 3D and regionally quantified by monitoring the signal changes in the lung parenchyma. Finally, image quality and quantitative ventilation values were compared to the standard 2D-SENCEFUL technique.

3D-UTE, combined with an automatic gating technique and SENCEFUL MRI, offered ventilation maps with high spatial resolution and SNR. Compared to the 2D method, UTE-SENCEFUL greatly improved the clinical quality of the structural images and the visualization of the lung parenchyma.

Through-plane motion, partial volume effects and ventilation artifacts were also reduced with a three-dimensional method for image registration.

UTE-SENCEFUL was also able to quantify regional ventilation and presented similar results to previous studies.

8 Zusammenfassung

In dieser Arbeit wurde eine 3D-UTE (ultrashort echo time) Sequenz mit SENCEFUL-MRI kombiniert. Die Sequenz wurde für einen 3 T MR-Scanner entwickelt und implementiert. Die 3D-UTE-Technik bestand aus einem nichtselektiven HF-Impuls, gefolgt von einer quasi-zufälligen Abtastung des k-Raums. Messungen in freier Atmung und ohne Kontrastmittel wurden bei gesunden Probanden und einem Patienten mit Lungenkrebs durchgeführt.

Zur Zuordnung der Daten zu verschiedene Atemphasen wurde eine Technik verwendet, die verschiedene Spulen mit hoher Signalkorrelation kombiniert. Die Ergebnisse wurden in einer in-vivo Messung bewertet und mit einem manuellen Ansatz der Spulenselektion verglichen.

Die Technik ermöglichte eine Visualisierung der Atembewegung und wurde als Referenz verwendet, um die erfassten Daten in mehrere Atemphasen zu segmentieren. Gradientenverzögerungen und Trajektorienfehler wurden mit der "Gradient Impulse Response Function - GIRF" korrigiert. Bei der Bildrekonstruktion kam Iteratives SENSE zum Einsatz.

Eine 3D-Bildregistrierung erlaubte es, Signaländerungen durch Bewegung zu eliminieren. Es erfolgte ein Vergleich der Ergebnisse mit einem 2D-Bildregistrierungsverfahren.

Die Lungenventilation wurde in 3D gemessen und anhand der Signaländerungen im Lungenparenchym quantifiziert. Schließlich, wurden die Werte für die Bildqualität und Lungenventilation mit der Standard-2D-SENCEFUL-Technik verglichen.

Die 3D-UTE-Sequenz in Kombination mit einer automatischen Gating-Technik und SENCEFUL-MRI, ermöglichte die Akquise von Ventilationskarten mit hoher räumlicher Auflösung und SNR. Im Vergleich zur 2D-Methode, verbesserte UTE-SENCEFUL die klinische Qualität der Morphologischen Bilder.

Bewegung, Partialvolumeneffekte und Ventilationsartefakte wurden ebenfalls mit einer dreidimensionalen Methode zur Bildregistrierung reduziert.

Insgesamt konnten mit der 3D-UTE Technik die Ergebnisse vorangegangener Studien reproduziert und die Bildqualität verbessert werden.

9 References

[1] NHS England. Diagnostic Imaging Dataset Statistical Release 2018. https://www.england.nhs.uk/statistics/statistical-work-areas/diagnostic-imaging-dataset/ (accessed March 4, 2019).

[2] Clinical-Imaging Board. CT Equipment , Operations , Capacity and Planning in the NHS Report from the Clinical Imaging Board 2015. https://www.sor.org/learning/document-library/ct-equipment-operations-capacity-and-planning-nhs/ (accessed March 4, 2019).

[3] Schauer DA, Linton OW. NCRP Report No. 160, Ionizing Radiation Exposure of the Population of the United States, medical exposure--are we doing less with more, and is there a role for health physicists? Health Physics. 2009.

[4] Bosch de Basea M, Salotti JA, Pearce MS, Muchart J, Riera L, Barber I, et al. Trends and patterns in the use of computed tomography in children and young adults in Catalonia - results from the EPI-CT study. Pediatric Radiology. 2016.

[5] Oikarinen H, Meriläinen S, Pääkkö E, Karttunen A, Nieminen MT, Tervonen O. Unjustified CT examinations in young patients. European Radiology. 2009.

[6] Clarke JC, Cranley K, Kelly BE, Bell K, Smith PHS. Provision of MRI can significantly reduce CT collective dose. The British Journal of Radiology. 2001.

[7] Brenner DJ. Slowing the Increase in the Population Dose Resulting from CT Scans. Radiation Research. 2010.

[8] Heye AK, Culling RD, Valdés Hernández M del C, Thrippleton MJ, Wardlaw JM. Assessment of blood-brain barrier disruption using dynamic contrast-enhanced MRI. A systematic review. NeuroImage: Clinical. 2014.

[9] Datta R, Sethi V, Ly S, Waldman AT, Narula S, Dewey BE, et al. 7T MRI Visualization of Cortical Lesions in Adolescents and Young Adults with Pediatric-Onset Multiple Sclerosis. Journal of Neuroimaging. 2017.

[10] Behl NGR, Gnahm C, Bachert P, Ladd ME, Nagel AM. Three-dimensional dictionary-learning reconstruction of 23 Na MRI data. Magnetic Resonance in Medicine. 2016.

[11] Anderson CE, Donnola SB, Jiang Y, Batesole J, Darrah R, Drumm ML, et al. Dual Contrast - Magnetic Resonance Fingerprinting (DC-MRF): A Platform for Simultaneous Quantification of Multiple MRI Contrast Agents. Scientific Reports. 2017.

[12] Malfair D, Beall DP. Imaging the Degenerative Diseases of the Lumbar Spine. Magnetic Resonance Imaging Clinics of North America. 2007.

[13] Kinner S, Pickhardt PJ, Riedesel EL, Gill KG, Robbins JB, Kitchin DR, et al. Diagnostic Accuracy of MRI Versus CT for the Evaluation of Acute Appendicitis in Children and Young Adults. American Journal of Roentgenology. 2017.

[14] Attwell D, Iadecola C. The neural basis of functional brain imaging signals. Trends in Neurosciences. 2002.

[15] Biederer J, Mirsadraee S, Beer M, Molinari F, Hintze C, Bauman G, et al. MRI of the lung (3/3)-current applications and future perspectives. Insights into Imaging. 2012.

[16] Zhang LJ, Zhou CS, Schoepf UJ, Sheng HX, Wu SY, Krazinski AW, et al. Dual-energy CT lung ventilation/perfusion imaging for diagnosing pulmonary embolism. European Radiology. 2013.

[17] Thieme SF, Becker CR, Hacker M, Nikolaou K, Reiser MF, Johnson TRC. Dual energy CT for the assessment of lung perfusion—Correlation to scintigraphy. European Journal of Radiology. 2008.

[18] Piai DB, Quagliatto R, Toro I, Cunha Neto C, Etchbehere E, Camargo E. The use of SPECT in preoperative assessment of patients with lung cancer. The European Respiratory Journal. 2004.

[19] Hochhegger B, Alves GRT, Irion KL, Fritscher CC, Fritscher LG, Concatto NH, et al. PET/CT imaging in lung cancer: indications and findings. Jornal Brasileiro de Pneumologia : Publicacao Oficial Da Sociedade Brasileira de Pneumologia

e Tisilogia. 2015.

[20] Johns CS, Swift AJ, Rajaram S, Hughes PJC, Capener DJ, Kiely DG, et al. Lung perfusion: MRI vs. SPECT for screening in suspected chronic thromboembolic pulmonary hypertension. Journal of Magnetic Resonance Imaging. 2017.

[21] Bauman G, Puderbach M, Deimling M, Jellus V, Chefd'hotel C, Dinkel J, et al. Non-contrast-enhanced perfusion and ventilation assessment of the human lung by means of fourier decomposition in proton MRI. Magnetic Resonance in Medicine. 2009.

[22] Fischer A, Weick S, Ritter CO, Beer M, Wirth C, Hebestreit H, et al. SElf-gated Non-Contrast-Enhanced FUnctional Lung imaging (SENCEFUL) using a quasi-random fast low-angle shot (FLASH) sequence and proton MRI. NMR in Biomedicine. 2014.

[23] Du J, Bydder GM. Qualitative and quantitative ultrashort-TE MRI of cortical bone. NMR in Biomedicine. 2013.

[24] Bydder GM, Fullerton GD, Young. IR. MRI of tissues with short T2s and T2*s. West Sussex: John Wiley and Sons; 2013.

[25] Weiger M, Brunner DO, Dietrich BE, Muller CF, Pruessmann KP. ZTE imaging in humans. Magnetic Resonance in Medicine. 2013.

[26] Faller A, Schünke M. The human body : an introduction to structure and function. Stuttgart: Georg Thieme Verlag; 2004.

[27] PixaBay. Health Medicine Anatomy - Free vector graphic on Pixabay n.d. https://pixabay.com/en/health-medicine-anatomy-lung-41508/ (accessed January 28, 2019).

[28] Cumming G, Bonsignore G, editors. Pulmonary Circulation in Health and Disease. 3rd ed. Geneva: Springer Science; 1980.

[29] Peacock AJ, Naeije R, Rubin LJ, editors. Pulmonary Circulation: Diseases and Their Treatment. 4th ed. Boca Raton: CRC Press; 2016.

[30] Wagner PD. The physiological basis of pulmonary gas exchange: implications for clinical interpretation of arterial blood gases. The European Respiratory Journal. 2015.

[31] Lutfi MF. The physiological basis and clinical significance of lung volume measurements. Multidisciplinary Respiratory Medicine. 2017.

[32] Hough A. Physiotherapy in respiratory care : an evidence-based approach to respiratory and cardiac management. 3rd ed. Cheltenham: Nelson Thornes; 2001.

[33] Luce JM, Pierson DJ, Tyler ML. Intensive respiratory care. W.B. Saunders; 1993.

[34] Overmoyer BA, McLaren CE, Brittenham GM. Uniformity of liver density and nonheme (storage) iron distribution. Archives of Pathology & Laboratory Medicine. 1987.

[35] Barber TW, Brockway JA, Higgins LS. The density of tissues in and about the head. Acta Neurologica Scandinavica. 1970.

[36] University of Washington Courses Web Server. TOXICOLOGY OF THE LUNG (2) 2003. http://courses.washington.edu/envh515/lung.html (accessed January 7, 2019).

[37] Yu J, Xue Y, Song HK. Comparison of lung T2* during free-breathing at 1.5 T and 3.0 T with ultrashort echo time imaging. Magnetic Resonance in Medicine. 2011.

[38] Zurek M, Bessaad A, Cieslar K, Crémillieux Y. Validation of simple and robust protocols for high-resolution lung proton MRI in mice. Magnetic Resonance in Medicine. 2010.

[39] Tibiletti M, Paul J, Bianchi A, Wundrak S, Rottbauer W, Stiller D, et al. Multistage three-dimensional UTE lung imaging by image-based self-gating. Magnetic Resonance in Medicine. 2015.

[40] Torres L, Kammerman J, Hahn AD, Zha W, Nagle SK, Johnson K, et al. “Structure-Function Imaging of Lung Disease Using Ultrashort Echo Time MRI.” Academic Radiology. 2019.

[41] Rahmer J, Börnert P, Groen J, Bos C. Three-dimensional radial ultrashort echo-time imaging with T2 adapted sampling. Magnetic Resonance in Medicine. 2006.

[42] Qian Y, Boada FE. Acquisition-weighted stack of spirals for fast high-resolution three-dimensional ultra-short echo time MR imaging. Magnetic Resonance in Medicine. 2008.

[43] Boada FE, Christensen JD, Gillen JS, Thulborn KR. Three-dimensional projection imaging with half the number of projections. Magnetic Resonance in Medicine. 1997.

[44] Tibiletti M, Bianchi A, Kjørstad Å, Wundrak S, Stiller D, Rasche V. Respiratory self-gated 3DUTE for lung imaging in small animal MRI. Magnetic Resonance in Medicine. 2016.

[45] Herrmann K-H, Krämer M, Reichenbach JR. Time Efficient 3D Radial UTE Sampling with Fully Automatic Delay Compensation on a Clinical 3T MR Scanner. PloS One. 2016.

[46] Nielles-Vallespin S, Weber MA, Bock M, Bongers A, Speier P, Combs SE, et al. 3D radial projection technique with ultrashort echo times for sodium MRI: Clinical applications in human brain and skeletal muscle. Magnetic Resonance in Medicine. 2007.

[47] Chang EY, Du J, Chung CB. UTE imaging in the musculoskeletal system. Journal of Magnetic Resonance Imaging : JMRI. 2015.

[48] Sheth V, Shao H, Chen J, Vandenberg S, Corey-Bloom J, Bydder GM, et al. Magnetic resonance imaging of myelin using ultrashort Echo time (UTE) pulse sequences: Phantom, specimen, volunteer and multiple sclerosis patient studies. NeuroImage. 2016.

[49] Grodzki DM, Jakob PM, Heismann B. Ultrashort echo time imaging using pointwise encoding time reduction with radial acquisition (PETRA). Magnetic Resonance in Medicine. 2012.

[50] Glover GH, Pauly JM. Projection Reconstruction Techniques for Reduction of Motion Effects in MRI. Magnetic Resonance in Medicine. 1992.

[51] Cha MJ, Park HJ, Paek MY, Stemmer A, Lee ES, Park S Bin, et al. Free-breathing ultrashort echo time lung magnetic resonance imaging using stack-of-spirals acquisition: A feasibility study in oncology patients. Magnetic

Resonance Imaging. 2018.

[52] Bankier AA, O'Donnell CR, Mai VM, Storey P, De Maertelaer V, Edelman RR, et al. Impact of lung volume on MR signal intensity changes of the lung parenchyma. Journal of Magnetic Resonance Imaging. 2004.

[53] Lujan AE, Larsen EW, Balter JM, Ten Haken RK. A method for incorporating organ motion due to breathing into 3D dose calculations. Medical Physics. 1999.

[54] Bailes DR, Gilderdale DJ, Bydder GM, Collins AG, Firmin DN. Respiratory ordered phase encoding (ROPE): a method for reducing respiratory motion artefacts in MR imaging. Journal of Computer Assisted Tomography. 1995.

[55] Larson AC, Kellman P, Arai A, Hirsch GA, McVeigh E, Li D, et al. Preliminary investigation of respiratory self-gating for free-breathing segmented cine MRI. Magnetic Resonance in Medicine. 2005.

[56] Larson AC, White RD, Laub G, McVeigh ER, Li D, Simonetti OP. Self-gated cardiac cine MRI. Magnetic Resonance in Medicine. 2004.

[57] Crowe ME, Larson AC, Zhang Q, Carr J, White RD, Li D, et al. Automated rectilinear self-gated cardiac cine imaging. Magnetic Resonance in Medicine. 2004.

[58] Ciet P, A W M Tiddens H, Morana G. Chest MRI: Morphological Imaging and Beyond. Magneton Flash. 2017.

[59] Kruger SJ, Fain SB, Johnson KM, Cadman R V, Nagle SK. Oxygen-enhanced 3D radial ultrashort echo time magnetic resonance imaging in the healthy human lung. NMR in Biomedicine. 2014.

[60] Bauman G, Bieri O. Matrix pencil decomposition of time-resolved proton MRI for robust and improved assessment of pulmonary ventilation and perfusion. Magnetic Resonance in Medicine. 2017.

[61] Bauman G, Lützen U, Ullrich M, Gaass T, Dinkel J, Elke G, et al. Pulmonary Functional Imaging: Qualitative Comparison of Fourier Decomposition MR Imaging with SPECT/CT in Porcine Lung. Radiology. 2011.

[62] Mendes Pereira L, Wech T, Weng AM, Kestler C, Veldhoen S, Bley TA, et al.

UTE-SENCEFUL: first results for 3D high-resolution lung ventilation imaging. Magnetic Resonance in Medicine. 2018.

[63] Lederlin M, Bauman G, Eichinger M, Dinkel J, Brault M, Biederer J, et al. Functional MRI using Fourier decomposition of lung signal: Reproducibility of ventilation- and perfusion-weighted imaging in healthy volunteers. European Journal of Radiology. 2013.

[64] Mierisová S, Ala-Korpela M. MR spectroscopy quantitation: a review of frequency domain methods. NMR in Biomedicine. 2001.

[65] Zapke M, Topf H-G, Zenker M, Kuth R, Deimling M, Kreisler P, et al. Magnetic resonance lung function--a breakthrough for lung imaging and functional assessment? A phantom study and clinical trial. Respiratory Research. 2006.

[66] Veldhoen S, Weng AM, Knapp J, Kunz AS, Stäb D, Wirth C, et al. Self-gated Non-Contrast-enhanced Functional Lung MR Imaging for Quantitative Ventilation Assessment in Patients with Cystic Fibrosis. Radiology. 2016.

[67] Zhang T, Cheng JY, Chen Y, Nishimura DG, Pauly JM, Vasanawala SS. Robust self-navigated body MRI using dense coil arrays. Magnetic Resonance in Medicine. 2016.

[68] Stich M, Mendes Pereira L, Wech T, M. Weng A, Ringler R, A. Bley TA, et al. Trajectory correction for a 3D-Ultrashort Echo Time (UTE) sequence using the gradient system transfer function. Proc. Intl. Soc. Mag. Reson. Med., Paris: 2018.

[69] Stich M, Wech T, Slawig A, Ringler R, Dewdney A, Greiser A, et al. Gradient waveform pre-emphasis based on the gradient system transfer function. Magnetic Resonance in Medicine. 2018.

[70] Pruessmann KP, Weiger M, Börnert P, Boesiger P. Advances in sensitivity encoding with arbitrary k-space trajectories. Magnetic Resonance in Medicine. 2001.

[71] Fessler JA. Michigan Image Reconstruction Toolbox (MIRT) 2016. https://web.eecs.umich.edu/~fessler/code/ (accessed March 2, 2018).

[72] Kroon D-J, Slump CH. MRI modalitiy transformation in demon registration.

2009 IEEE International Symposium on Biomedical Imaging: From Nano to Macro, IEEE; 2009.

[73] Myronenko A, Xubo Song. Intensity-Based Image Registration by Minimizing Residual Complexity. IEEE Transactions on Medical Imaging. 2010.

[74] Robson PM, Grant AK, Madhuranthakam AJ, Lattanzi R, Sodickson DK, McKenzie CA. Comprehensive quantification of signal-to-noise ratio and *g* -factor for image-based and *k* -space-based parallel imaging reconstructions. Magnetic Resonance in Medicine. 2008.

[75] Sheppard A, Chen Y-C, Salvi R. MRI Noise and Hearing Loss. The Hearing Journal. 2018.

[76] Johnson KM, Fain SB, Schiebler ML, Nagle S. Optimized 3D ultrashort echo time pulmonary MRI. Magnetic Resonance in Medicine. 2013.

10 List of figures

Figure 1. Anterior view of the upper and lower airways. 16

Figure 2. Bronchiole, capillaries and alveoli. 17

Figure 3. Schematic of the oxygen transport pathway showing the principal structures and their physiological functions. 18

Figure 4. Standard lung volumes and capacities from a spirometer trace 20

Figure 5. Microscopic image of the lung parenchyma 22

Figure 7. Two dimensional cartesian and radial k-space trajectories. 23

Figure 6. Ultrashort echo time sequences diagrams for 2D and 3D acquisitions 25

Figure 8. Simulation of the position of the diaphragm. 28

Figure 9. Simulation of the contribution of the cardiac and breathing motions to the MR signal. 29

Figure 10. Spectral separation of the cardiac and breathing motions in the frequency domain. 30

Figure 11. Breathing phases reconstructed using an Img-SG approach. 32

Figure 12. The position of the diaphragm during a free-breathing measurement monitored with an Img-SG approach 32

Figure 13. DC signal from a single coil element positioned close to the diaphragm. 34

Figure 14. Morphological CT in coronal view and perfusion maps of a patient with a cystic parenchymal defect 38

Figure 15 - Ventilation-weighted and perfusion-weighted images generated with MP and standard FD method 40

Figure 16. Illustration of the DC signal extracted from a coil element close to the diaphragm and the corresponding gating process 42

Figure 17. DC signal measured with a coil element sensible to the cardiac motion .43

Figure 18. Different respiratory and cardiac phases measured from a healthy subject 44

Figure *19*. Comparison of SENCEFUL with DCE-MRI and Fourier decomposition. 46

Figure 20. K-space trajectory and acquisition scheme 49

Figure 21. Coil clustering algorithm. 52

Figure 22. Gating process illustration 54

Figure 23. Lung segmentation 58

Figure 24. FLASH sequence diagram 59
Figure 25. Comparison between SENSE and traditional gridding. 65
Figure 26. Filtered DC signal extracted with the coil clustering algorithm 67
Figure 27. DC signal from a manually chosen coil compared to a coil-cluster. 68
Figure 28. Comparison of coil clustering and manual selection of the DC signal 69
Figure 29. Gating signal from a patient with lung cancer 70
Figure 30. Reconstructed breathing phases from 2D-FLASH and 3D-UTE 72
Figure 31. SNR maps from similar coronal slices 73
Figure 32. 2D and 3D image registration comparison 76
Figure 33. Ventilation-weighted maps from a healthy subject. 78
Figure 34. Ventilation-weighted maps from a patient with lung cancer. 81

11 List of Tables

Table 1. 3D-UTE measurement parameters 50

Table 2. 2D-FLASH acquisition parameters.. 60

Table 3. Average quantitative weighted ventilation values from the group of healthy subjects, assessed with UTE-SENCEFUL and 2D-SENCEFUL. 79

Table 4. Quantitative weighted ventilation values assessed using UTE-SENCEFUL and 2D-SENCEFUL for a single patient with lung cancer 82

Acknowledgements

I would like to thank the National Council for Scientific and Technological Development (CNPq), the Graduate School of Life Science (GSLS) and the University Clinic of Würzburg for the financial support.

I would like to express my deep gratitude to Prof. Dr. Herbert Köstler for welcoming me into his group and for offering the perfect environment for the development of this research.

I am also thankful for the members of my thesis committee, Prof. Dr. Michael Laßmann, Dr. Thorsten Klink and Dr. Simon Veldhoen, for the provided guidance.

I wish to acknowledge Dr. Tobias Wech and Dr. Andreas M. Weng for their constant resourcefulness, patience and support throughout my study.

My special thanks are extended to the current and past members of the Experimental Radiology group, in special to Dr. Anne Slawig, Michael Braun, Manuel Stich, Phillip Eirich, Julian Richter, Manuel Köblinger, Dr. Fabian Hilbert, Katharina Rath, Juliana Bibiano, Johannes Portmann and Susanne Gaul for all the pleasant hours spent together.

I thank my family, in special my parents, José Carlos B. Pereira and Maria de Fátima E. M. Pereira for their constant encouragement and emotional support. I also thank my brother, Lincon Vinícius. M. Pereira, for the unconditional love and friendship.

A special thanks to Katrin Lutterbüse, Benjamin Lambour, Cristina Perpiña Viciano, Jerome Becan and Jéssica S. Machado for not only being my friends, but also my family during the past few years.

And last, but not least, I am grateful for all the love and support given by my husband, Alan Tonello Borba. Thank you for being there for me on every step of this journey.

Publications

Papers

- L. Mendes Pereira, H. J. Khoury, M. E. A. Andrade, V. S. M. Barros, D. L. Cutajar, A. B. Rosenfeld. **Evaluation of the MOSkin dosimeter for diagnostic X-ray CT beams**. Physica Medica. Accepted on the 28th of March 2019.

- L. Mendes Pereira, T. Wech, A.M. Weng, C. Kestler, S. Veldhoen, T.A. Bley, H. Köstler. **UTE-SENCEFUL: first results for 3D high-resolution lung ventilation imaging**. Magnetic Resonance in Medicine, 2018;00:1–10. https://doi.org/10.1002/mrm.27576

Conference Proceedings

- L. Mendes Pereira, A. M. Weng, T. Wech, S. Veldhoen, T. A. Bley, H. Köstler. **UTE-SENCEFUL with a coil clustering algorithm for automatic DC gating**. Proceedings of the annual meeting of the International Society for Magnetic Resonance in Medicine. Montreal, 2019.

- J. F. Heidenreich, A. M. Weng, C. Metz , L. Mendes Pereira , T. Benkert, J. Pfeuffer, T. A. Bley , H. Köstler, S. Veldhoen. **Comparison of Quantitative Pulmonary Ventilation Imaging using 3D-UTE under breath-holding and free-breathing in patients with structural lung disease at 3T**. Proceedings of the annual meeting of the International Society for Magnetic Resonance in Medicine. Montreal, 2019.

- L. Mendes Pereira, A. M. Weng, T. Wech, S. Veldhoen, T. A. Bley, H. Köstler. **UTE-SENCEFUL: high resolution 3D ventilation weighted maps**. Proceedings of the annual meeting of the International Society for Magnetic Resonance in Medicine. Paris, 2018.

- M. Stich, L. Mendes Pereira, T. Wech, A. M. Weng, R. Ringler, T. A. Bley, H. Köstler. **Trajectory correction for a 3D-Ultrashort Echo Time (UTE) sequence using the gradient system transfer function.** Proceedings of the annual meeting of the International Society for Magnetic Resonance in Medicine. Paris, 2018.

- L. Mendes Pereira, A. Weng, T. Wech, C. Kestler, S. Veldhoen, T. A. Bley, H. Köstler. **UTE-SENCEFUL: high resolution functional lung imaging.** Proceedings of the European Society for Magnetic Resonance in Medicine & Biology, Barcelona, 2017.

- L. Mendes Pereira, T. Wech, A. Weng, A. S. Kunz, S. Veldhoen, T. A. Bley, H. Köstler. **Self-gated ultra-short echo time lung MRI for quantitative ventilation assessment.** Proceedings of the annual meeting of the International Society for Magnetic Resonance in Medicine. Hawaii, 2017.

- A. M. Weng , T. Wech , L. Mendes Pereira , S. Veldhoen , A. S. Kunz , T. A. Bley , H. Köstler. **Optimizing data efficiency in SENCEFUL-based lung perfusion studies.** Proceedings of the annual meeting of the International Society for Magnetic Resonance in Medicine. Hawaii, 2017.

Affidavit / Eidesstattliche Erklärung

Affidavit

I hereby confirm that my thesis entitled *Morphological and Functional Ultrashort Echo Time (UTE) Magnetic Resonance Imaging of the Human Lung* is the result of my own work. I did not receive any help or support from commercial consultants. All sources and / or materials applied are listed and specified in the thesis.

Furthermore, I confirm that this thesis has not yet been submitted as part of another examination process neither in identical nor in similar form.

Place, Date

Signature

Eidesstattliche Erklärung

Hiermit erkläre ich an Eides statt, die Dissertation *Morphologische und funktionelle Magnetresonanztomographie der menschlichen Lunge mit ultrakurzen Echozeiten (UTE)* eigenständig, d.h. insbesondere selbständig und ohne Hilfe eines kommerziellen Promotionsberaters, angefertigt und keine anderen als die von mir angegebenen Quellen und Hilfsmittel verwendet zu haben.

Ich erkläre außerdem, dass die Dissertation weder in gleicher noch in ähnlicher Form bereits in einem anderen Prüfungsverfahren vorgelegen hat.

Ort, Datum

Unterschrift

Curriculum Vitae